



**HAL**  
open science

## Investigating the nature of active forces in tissues reveals how contractile cells can form extensile monolayers

Lakshmi Balasubramaniam, Amin Doostmohammadi, Thuan Beng Saw, Gautham Hari Narayana Sankara Narayana, Romain Mueller, Tien Dang, Minnah Thomas, Shafali Gupta, Surabhi Sonam, Alpha S Yap, et al.

### ► To cite this version:

Lakshmi Balasubramaniam, Amin Doostmohammadi, Thuan Beng Saw, Gautham Hari Narayana Sankara Narayana, Romain Mueller, et al.. Investigating the nature of active forces in tissues reveals how contractile cells can form extensile monolayers. *Nature Materials*, 2021, 20 (8), pp.1156-1166. 10.1038/s41563-021-00919-2 . hal-03388494

**HAL Id: hal-03388494**

**<https://hal.science/hal-03388494v1>**

Submitted on 20 Oct 2021

**HAL** is a multi-disciplinary open access archive for the deposit and dissemination of scientific research documents, whether they are published or not. The documents may come from teaching and research institutions in France or abroad, or from public or private research centers.

L'archive ouverte pluridisciplinaire **HAL**, est destinée au dépôt et à la diffusion de documents scientifiques de niveau recherche, publiés ou non, émanant des établissements d'enseignement et de recherche français ou étrangers, des laboratoires publics ou privés.

1 Investigating the nature of active forces in tissues  
2 reveals how contractile cells can form extensile  
3 monolayers

4 Lakshmi Balasubramaniam,<sup>1\*</sup> Amin Doostmohammadi,<sup>2,3\*</sup>  
Thuan Beng Saw,<sup>4,5</sup> Gautham Hari Narayana Sankara Narayana,<sup>1</sup>  
Romain Mueller,<sup>3</sup> Tien Dang,<sup>1</sup> Minnah Thomas,<sup>4</sup> Shafali Gupta,<sup>6</sup> Surabhi Sonam,<sup>1,7</sup>  
Alpha S. Yap,<sup>6</sup> Yusuke Toyama,<sup>4</sup> René-Marc Mège,<sup>1</sup> Julia Yeomans,<sup>3</sup> Benoît Ladoux<sup>1</sup>

<sup>1</sup>Institut Jacques Monod (IJM), CNRS UMR 7592 et Université de Paris,  
75013 Paris, France,

<sup>2</sup>Niels Bohr Institute, University of Copenhagen,  
Blegdamsvej 17, 2100 Copenhagen, Denmark

<sup>3</sup>The Rudolf Peierls Centre for Theoretical Physics, University of Oxford,  
Parks Road, Oxford OX1 3PU, UK

<sup>4</sup>Mechanobiology Institute (MBI), National University of Singapore, Singapore, 117411

<sup>5</sup> National University of Singapore, Department of Biomedical Engineering,  
4 Engineering Drive 3, Engineering Block 4, # 04-08, Singapore, 117583

<sup>6</sup>Division of Cell and Developmental Biology, Institute for Molecular Bioscience,  
The University of Queensland, St. Lucia, Brisbane, QLD 4072, Australia

<sup>7</sup>Present address: D Y Patil International University, Akurdi, Pune, India

\*These authors contributed equally to this work

5 **Actomyosin machinery endows cells with contractility at a single cell level.**  
6 **However, within a monolayer, cells can be contractile or extensile based on**  
7 **the direction of pushing or pulling forces exerted by their neighbours or on**  
8 **the substrate. It has been shown that a monolayer of fibroblasts behaves as a**  
9 **contractile system while epithelial or neural progenitor monolayers behave as**  
10 **an extensile system. Through a combination of cell culture experiments and in**  
11 **silico modeling, we reveal the mechanism behind this switch in extensile to con-**  
12 **tractile as the weakening of intercellular contacts. This switch promotes the**  
13 **buildup of tension at the cell-substrate interface through an increase in actin**  
14 **stress fibers and traction forces. This is accompanied by mechanotransductive**  
15 **changes in vinculin and YAP activation. We further show that contractile and**  
16 **extensile differences in cell activity sort cells in mixtures, uncovering a generic**  
17 **mechanism for pattern formation during cell competition, and morphogenesis.**

## 18 **Main text**

19 The ability of cell monolayers to self-organize, migrate and evolve depends crucially on the in-  
20 terplay between cell-matrix and cell-cell interactions [1–4] which controls various phenomena  
21 including tissue morphogenesis [5, 6], epithelial-mesenchymal transition [1], wound healing  
22 and tumor progression [7]. Cells are active systems, engines that operate away from thermal  
23 equilibrium, transducing chemical energy into motion. Single isolated cells generate contractile  
24 force dipoles: the resultant of the forces due to actomyosin contraction, pulling on focal adhe-  
25 sion sites on the substrate, is typically a pair of approximately equal and opposite forces acting  
26 inwards along the cellular long axis [8] (Figure 1a). It is reasonable to expect that contractile  
27 particles also generate contractile behaviour in the monolayer [9]. However, at the collective  
28 cell level, epithelial monolayers [10, 11] and a monolayer of neural progenitor cells display

29 extensile behaviour [12] i.e. the net force from the neighbours and substrate interaction act  
30 to elongate the cell further along its long axis (Figure 1b inset). This immediately poses the  
31 question of how such a crossover occurs as the emergence of such differences in active be-  
32 haviour may be crucial in understanding biological processes such as tissue homeostasis, cell  
33 competition and self organization [13].

34 The extensility or contractility within cell populations are based on force balance as shown in  
35 Figure 1b and this can be determined by looking at the structure of flow fields around topological  
36 defects. Topological defects are singular points in the orientation field of the cell monolayers,  
37 where the orientation of cells were defined as the direction of their long axis (see Methods).  
38 Having identified the orientation of cells, we use the winding number parameter to identify the  
39 location of topological defects, using an automated defect detection method [10]. In a cellular  
40 monolayer two types of topological defects predominate: comet-shaped defects and trefoils  
41 (Figure 1c), which correspond to topological defects in nematic liquid crystals with charges  
42  $+1/2$  and  $-1/2$ , respectively [9–12, 14].

43 Of relevance here in active systems, the active nature of cells results in a directed motion of the  
44 comet shaped defects. For extensile systems, the defects move in the direction of the head of  
45 the comet, while topological defects in contractile systems move towards the comet tail (Fig-  
46 ure 1b). Thus, we measured the average flow field around the comet defects in Madin-Darby  
47 Canine Kidney Wild-Type (MDCK WT) monolayers using Particle Image Velocimetry (PIV).  
48 The flow and orientation field were obtained from time lapse imaging after they reached con-  
49 fluency and before the cells became isotropic as the monolayers grew too dense. The results  
50 show clearly that the comet-shaped defects move in the tail-to-head direction (Figure 1d,e, Sup-  
51 plementary Figure 1a, c, Video 1), indicating that at a collective level the MDCK monolayer  
52 behaves as an extensile active system despite forming contractile dipoles at a single cell level

53 (Figure 1a). The extensile behaviour of comet-shaped defects has been recently reported for  
54 Human Bronchial Epithelial Cells (HBEC) as well [11], indicating it to be a property of ep-  
55 ithelial monolayers. By contrast, the flow field around comet shaped defects in a monolayer  
56 of fibroblasts has an opposite flow direction - from head-to-tail of the comet - indicating that  
57 fibroblasts behave as a contractile system at the collective level (Supplementary Figure 2a), in  
58 agreement with previous studies [9]. This difference in the direction of motion of defects is  
59 also reflected in the patterns of strain rates around the defects. While strain rate along the tail-  
60 to-head direction ( $yy$ -strain rates) show negative values at the head of a comet-shaped defect  
61 in MDCK WT monolayers indicating the presence of compression (Figure 1d), this is reversed  
62 for a monolayer of fibroblasts, where the  $yy$ -strain rate at the defect head is positive, indicating  
63 extensional deformation (Supplementary Figure 2a). But what causes epithelial cells to behave  
64 as an extensile system at the collective level, and mesenchymal cells as a contractile system,  
65 and what are the consequences during tissue organization are not well understood.

66 One fundamental difference between epithelial and mesenchymal cells is the ability of epithe-  
67 lial cells to form strong cell-cell adhesions through E-cadherin based junctional complexes,  
68 responsible for active intercellular force transmission [15]. In order to discern the origin of ex-  
69 tensile behaviour at a collective level, we performed laser ablation experiments on MDCK WT  
70 monolayers (Supplementary Figure 3a,b), where we observed higher recoil at shorter junctions  
71 in comparison to long junctions. These results highlight that the smaller cortical tension along  
72 long junctions gives rise to a tension distribution that leads to an extensile stress on the cell  
73 further elongating it. We therefore asked if weakening this intercellular adhesion in epithelial  
74 cells results in a (mesenchymal-like) contractile behaviour at the collective level. To test this,  
75 we inactivated the E-cadherin gene in MDCK cells using CRISPR-Cas9 which was validated  
76 through immunostaining and western blot analysis (Supplementary Figure 4a,b,h). MDCK E-  
77 cadherin Knock-Out (E-cad KO) cells can still maintain their contacts through another form of

78 cadherin (cadherin 6), albeit with a significantly weaker adhesion strength as observed through  
79 the reduced level of  $\beta$ -catenin at adherens junctions (Supplementary Figure 4a,b,h), while still  
80 being able to form tight junctions (Supplementary Figure 4a). Strikingly, in these E-cad KO  
81 monolayers, the average flow field around comet defects switches direction compared to WT  
82 monolayers (Figure 1d and e, Supplementary Figure 1a,d, Video 2), indicating a contractile  
83 behaviour at the collective level similar to that of fibroblasts where the comet shaped defects  
84 move towards the tail direction (Supplementary Figure 2). This change in direction of the flow  
85 field around the defect was accompanied by changes in the average strain rate patterns which  
86 are positive (extensile deformation) around the head of a comet shaped defect in E-cadherin  
87 KO monolayers in comparison to WT monolayers where the strain rate is negative (compressive  
88 deformation) around the head of the defect (Figure 1d). Therefore, epithelial monolayers  
89 behave as an extensile system due to the presence of strong cell-cell adhesions and loosening  
90 this adhesion by removing E-cadherin results in a contractile behaviour.

91 In order to check that this switch from extensile to contractile behaviour is not only specific  
92 to MDCK cells, we further validated the results by perturbing cell-cell contacts in the hu-  
93 man breast cancer cell line MCF7A, where depleting E-cadherin by RNAi (Supplementary  
94 Figure 4e) changed the behaviour from an extensile to a contractile system (Supplementary Fig-  
95 ure 4f,g). We then validated that this switch was not a clonal effect by re-expressing E-cadherin  
96 which restored collective extensile behaviour to MDCK E-cad KO cells (Supplementary Fig-  
97 ure 5a). Moreover, the total defect density within the monolayer of MDCK WT and MDCK  
98 E-cad KO cells did not reveal changes in the density of defects between WT and E-cad KO  
99 monolayers (Supplementary Figure 5b) indicating that the average distance between the defects  
100 and defect-defect interactions are not affected by E-cadherin removal. Furthermore, measuring  
101 average flows around  $-1/2$  (trefoil) defects did not show any significant difference between  
102 WT and E-cad KO monolayers (Supplementary Figure 2b, and 5c). This is consistent with both

103 simulations (Supplementary Figure 5d) and theories of active nematics [16, 17], which show  
104 that difference in activity affects the self-propulsion of  $+1/2$  defects, while not altering the ve-  
105 locity field of  $-1/2$  defects. Indeed, comparing the Mean-Square-Displacement (MSD) from  
106 defect trajectories in WT and E-cad KO monolayers clearly indicates that while  $+1/2$  defects  
107 have propulsive behaviour and move faster in WT monolayers, the motion of  $-1/2$  defects is  
108 diffusive in both conditions (Supplementary Figure 5e).

109 We next checked whether the extensile to contractile crossover could be the impact of a change  
110 in the behaviour of individual cells. However, based on our traction force data, both single  
111 isolated WT and single isolated E-cad KO cells showed contractile behaviour with the forces  
112 directed inwards along their elongation axes as cells pulled on the substrate (Figure 1a). This  
113 indicates that removing E-cadherin does not change the contractile pattern (intracellular stress)  
114 of single cells (Supplementary Figure 6a). Therefore, the change from contractile to extensile  
115 behaviour at the collective level can be linked to the presence of E-cadherin which mediates  
116 force transmission between neighbouring cells through intercellular interactions.

117 In order to better discern the competition between intracellular contractile stresses (generated by  
118 the actomyosin machinery throughout the cell) and the intercellular stresses (due to neighbour  
119 interactions), we varied these two stresses independently using a cell-based model. The model  
120 is based on a phase-field formulation [18] that captures the deformation of individual cells, and  
121 has recently been shown to reproduce the formation of topological defects in MDCK monolay-  
122 ers, along with their associated flow field and stress patterns [19]. In a similar manner as in the  
123 experimental analysis, where the orientation of cells were identified through their long axis, in  
124 the model a shape tensor,  $S$ , characterizes the magnitude and direction of cell elongation (Fig-  
125 ure 2a). This parameter continuously evolves with the deformation of cells as they push/pull on  
126 their neighbours within the monolayer. Following our recent work [19], intercellular stresses

127 are defined to be proportional to the shape tensor which allows us to model extensile stresses  
128 at the cell-cell contacts (Figure 2a). This form of modeling was inspired by previous studies  
129 on adherens junctions and actomyosin interaction which showed that force transduction at the  
130 junction can modify the actomyosin network and in turn the cell shape [20] and was experimen-  
131 tally validated on MDCK WT monolayers through laser ablation experiments where shorter  
132 junctions were under higher tension (higher recoil velocity) in comparison to longer junctions  
133 which were under lower tension (lower recoil velocity) (Supplementary Figure 3a,b). In ad-  
134 dition, an intracellular stress is defined to mimic internal stresses generated by acto-myosin  
135 complexes within the individual cells (see Methods for the details of the model). The effect  
136 of E-cadherin removal is thus captured in the model by tuning down the intercellular stresses.  
137 Just as in the experiments both comet-shaped and trefoil topological defects ( $+1/2$  and  $-1/2$   
138 charges, respectively) are found in the orientation field of the monolayer (Figure 2b) and the  
139 average flow fields and strain rate maps around comet shaped defects match those measured  
140 for the WT cells (Figure 2c). More importantly, we found that lowering intercellular stresses  
141 switched flow direction around comet-shaped topological defects and strain rates in agreement  
142 with experimental results of E-cad KO (Figure 2b and c). Quantitative analysis of the simu-  
143 lations showed that reducing the intercellular stresses results in slower dynamics characterized  
144 by a smaller root mean square (rms)-velocity (Figure 2d) and generates less correlated patterns  
145 of motion characterized by a smaller velocity correlation length (Figure 2e). Moreover, due to  
146 the dipolar symmetry of intercellular stresses in the model, simulation results predict that the  
147 switch from extensile to contractile behaviour does not alter the isotropic stress patterns, i.e.,  
148 tension (positive isotropic stress) and compression (negative isotropic stress) around the defects  
149 (Figure 3a), when intercellular stresses are reduced.

150 To test the predictions of the model we first experimentally studied the effect of E-cad KO on  
151 the stress patterns around topological defects and collective motion of cells. Using traction

152 force microscopy, we obtain traction forces in the monolayer, from which we infer the associ-  
153 ated stress patterns using Bayesian Inversion Stress Microscopy (BISM) [21]. Using a similar  
154 approach as strain rate measurements around defects, we are able to compute the average stress  
155 fields around comet shaped defects. Our experiments agreed with the simulations in showing no  
156 difference in the average isotropic stress patterns around comet shaped defects between the WT  
157 (Figure 3b) and E-cad KO monolayers (Figure 3c), while they still show a difference in their  
158 flow field (Supplementary Figure 6b) [10], indicating that the tension and compression around  
159 defects are primarily controlled by local cellular organization and elongation, and not the flow  
160 field around them. Moreover, measuring the velocity correlation function [22], we found it to  
161 be consistent with the numerical predictions whereby removing E-cadherin reduces the cor-  
162 relation length compared to the WT monolayers (Figure 3d). This is also in agreement with  
163 previous reports which demonstrate a reduction in velocity correlation length of mesenchymal  
164 cells with respect to epithelial cells [22]. Interestingly, by performing rescue experiments to  
165 put E-cadherin back, we found an increase in velocity correlation length (Figure 3d) which was  
166 very close to that of WT monolayers. This indicates that the perturbation of junctional protein  
167 E-cadherin can be used as an effective way of tuning the collective contractility and extensibility  
168 of the epithelial monolayer.

169 Comparing the average velocities in the monolayers with and without E-cadherin also agreed  
170 with the model's prediction that the velocity of the monolayer is reduced upon E-cadherin de-  
171 pletion (Figure 3e) at similar density. Interestingly, traction force microscopy measurements re-  
172 vealed that this reduction in velocity is accompanied by a significant (about three fold) increase  
173 in the average traction forces that E-cad KO monolayers exert on their underlying substrate  
174 in comparison to WT monolayers (Figure 3f). Furthermore, we compared average cell areas  
175 within the monolayer for both WT and E-cad KO monolayers and did not notice an appreciable  
176 difference in spreading area, although for both WT and E-cad KO monolayers the average cell

177 spreading area reduced over time (Figure 3g). In contrast, the aspect ratio of cells within the  
178 WT monolayers reduced over time while the aspect ratio of cells within E-cad KO monolayers  
179 did not change over time (Figure 3g). These measurements of velocity reduction, traction force  
180 increase, and changes in aspect ratio in the monolayers without E-cadherin, combined together,  
181 hinted that the cell-substrate interaction increased as the cell-cell interaction was weakened,  
182 indicating a possible cross-talk between intracellular and intercellular interactions as reported  
183 previously [23, 24] .

184 To test this, and based on previous studies that showed changes in cellular response to substrate  
185 adhesions [25, 26] , we asked if the increase in the average traction force of E-cad KO mono-  
186 layers was a result of changes in their mechanotransductive response. Using actin staining we  
187 first checked for changes in the organization of stress fibers in the cells within a monolayer,  
188 as stress fiber formation is an important determinant of force generation by cells on a sub-  
189 strate [27, 28]. Indeed, comparing actin staining of WT and E-cad KO monolayers, we found a  
190 considerable increase in stress fibers in the absence of E-cadherin (Figure 4a). Concomitantly,  
191 phosphomyosin staining of WT and E-cad KO monolayers showed an increase in the number  
192 of phosphomyosin light chain (pMLC2) fibers (Figure 4a) generated at the basal surface within  
193 E-cad KO cells. Western blot analyses further revealed an increase in the total level of myosin  
194 light chains (MLC2) (Supplementary Figure 4c,h). Considering these results we reasoned that  
195 inhibiting cell contractility in E-cad KO cells may alter their active behaviour. Upon treatment  
196 with a mild dose of blebbistatin (5  $\mu$ M), an inhibitor of Myosin II (Supplementary Figure 7a)  
197 E-cad KO monolayers still behave as a contractile system. However, a higher dose (20  $\mu$ M)  
198 of blebbistatin (Supplementary Figure 7b) or 25  $\mu$ M of Y27632, an inhibitor of ROCK 1 and  
199 2 (Supplementary Figure 7c), resulted in a switch in behaviour from a contractile to that of an  
200 extensile system as summarized in Supplementary Table1. As control, we showed that similar  
201 treatments did not affect the extensile behaviour of the WT monolayers (Supplementary Table 1,

202 Supplementary Figure 7d and e). We then measured the traction forces exerted by cells when  
203 treated with 20  $\mu$ M blebbistatin. As reported previously [29], treatment of both WT and E-cad  
204 KO monolayers with 20  $\mu$ M of blebbistatin results in a drastic reduction of traction forces (Fig-  
205 ure 4b). This reinforces the importance of cell substrate interaction in dictating the contractile  
206 behaviour of E-cad KO monolayers. Thus, removing E-cadherin not only reduces the extensile  
207 intercellular stresses, it also increases the intrinsic contractility (intracellular stress) generated  
208 by cells at the cell-substrate interface.

209 Since focal adhesions (FAs) are known to be mechanosensors at cell-matrix interface [30], we  
210 then investigated the assembly of FAs in E-cad KO and WT monolayers. By using paxillin  
211 staining to determine changes in FAs, we showed a marked increase both in length, and area  
212 within the cells (Figure 4c) in the E-cad KO monolayers in comparison to the WT monolayers.  
213 More importantly, we found that the E-cad KO modified the subcellular localization of vinculin,  
214 a protein which is known to respond and transmit force from both integrin and cadherin based  
215 adhesion complexes [31, 32]. While the total level of vinculin remained unchanged in both  
216 WT and E-cad KO monolayers (Supplementary Figure 4d,h), the localization of vinculin was  
217 altered, whereby vinculin was mostly present at the cell-cell junctions in WT monolayers, but  
218 basally located in E-cad KO monolayers (Figure 4d). We further verified if all paxillin positive  
219 focal adhesions were vinculin positive in both WT and E-cad KO monolayers and observed a  
220 strong correlation between them (Pearson's coefficient of 0.8842 and 0.8843 for WT and E-cad  
221 KO) as shown in Supplementary Figure 8, reiterating our observed increase in cell-substrate  
222 interaction in the absence of E-cadherin.

223 Since Yes-associated protein (YAP) transcriptional activity is also known to modify cell me-  
224 chanics, force development and FA strength [33], we investigated the localization of YAP within  
225 E-cad KO monolayers. Interestingly, we found that YAP was predominantly localized to the nu-

226 cleus in E-cadherin KO monolayers (Figure 4e), which corresponds to the active state of YAP.  
227 This is in agreement with previous studies that reported an activation of YAP through nuclear  
228 accumulation in the absence of E-cadherin or in well spread cells [34, 35]. Taken together, our  
229 results show that removing E-cadherin enhances the formation of stress fibers, promotes YAP  
230 activation, alters viculin localization, and leads to a marked increase in the formation of focal  
231 adhesions and their linkage to the substrate, in turn triggering a contractile behaviour.

232 Our force measurements together with acto-myosin activity and adhesion patterns establish that  
233 the extensile or contractile nature of epithelial cells at a collective level relies on the interplay be-  
234 tween active stresses at cell-cell and cell-matrix interfaces. To further explore this crossover we  
235 plated cells on a soft (2.3 kPa) polyacrylamide (PA) gels, recalling that cellular responses on soft  
236 substrates leads to lower contractility and less stable focal adhesions [36]. MDCK WT mono-  
237 layers remained extensile regardless of substrate stiffness (Supplementary Figure 9a), while  
238 E-cad KO cells switched from contractile to extensile behaviour on a soft substrate (around 2.3  
239 kPa) (Supplementary Figure 9b). Taken together, these experiments show that tuning cell-cell  
240 and cell-substrate adhesion can result in a switch between extensile and contractile behaviour  
241 of cell monolayers further validating our observatin that blebbistatin treatment drastically re-  
242 duced traction forces (Figure 4d) and switched the behaviour of E-cad KO monolayers from  
243 contractile to extensile. It is possible in the simulations to further explore this crossover by con-  
244 tinuously varying the strength of intra- and inter-cellular stresses, independently. The results are  
245 summarized in a stability-phase diagram that classifies the monolayer behaviour as extensile or  
246 contractile based on the direction of the defect motion (Supplementary Figure 10a). The non-  
247 symmetric structure of the stability-diagram further highlights the different impacts of intra-  
248 and inter-cellular stresses on the direction of defect motion. In our simluations, while intracel-  
249 lular stresses act within single cells and are along the direction of cell polarity, the intercellular  
250 stresses arise in between neighboring cells and are proportional to the cell deformation. As

251 such, intercellular stresses can reinforce themselves: small cell deformations lead to intercellu-  
252 lar stresses that further enhance cell deformation, generating stronger intercellular stresses. We  
253 conjecture that this bootstrap mechanism results in intercellular stresses to more strongly affect  
254 the collective behavior of the monolayer compared to their intracellular counterparts.

255 Based on this difference in contractile and extensile behaviour we then used the model to sim-  
256 ulate the interaction between the extensile and contractile systems. The results showed that  
257 cells were able to separate out into two different phases over time when mixed at 50-50 ratio  
258 (Figure 5a and Supplementary Figure 10b, Video 3), where extensile cells were surrounded by  
259 contractile ones. We were able to replicate this experimentally (Figure 5b and Supplementary  
260 Figure 10c, Video 4) whereby WT and E-cad KO cells separate out into two different phases  
261 with WT (extensile) cells surrounded by E-cad KO (contractile) cells when plated at a 50-50 ra-  
262 tio (Figure 5a). While thermodynamic mechanisms such as differential adhesion and difference  
263 in line tension between two cell types have been shown to govern phase separation in 3D cell  
264 aggregates [37–39], active cell sorting in monolayers with strong substrate adhesion, has not  
265 been directly observed to the best of our knowledge. We, therefore, sought to further explore  
266 the possible distinctions between the cell sorting, as observed here, and the well-established  
267 differential adhesion and differential line tension hypotheses. To this end, we first quantified  
268 the degree of phase separation by measuring the mixing-index of a mixture of WT and E-cad  
269 KO cells defined as the number of homotypic neighbours over the total number of cells [40,  
270 41]. In the segregation mechanism based on differential line tension this mixing-index grows  
271 with a power-law exponent with time and approaches one [41]. However, as evident from both  
272 experiments and simulations, the mixing-index in our system saturates and complete phase sep-  
273 aration is never obtained (Figure 5a and b). We conjecture that this is partly because of strong  
274 cell-substrate adhesion that dominates over any possible difference in line tensions and also  
275 due to a fundamental difference between activity-driven phase separation and thermodynamic

276 mechanisms. In addition, phase separation based on differential line tension posits that – in-  
277 dependent of the asymmetry of the binary mixture - the phase with higher line tension always  
278 forms aggregates that are enveloped by the cells with lower line tension to minimize the free  
279 energy of the mixture [37, 39].

280 To test this, we performed mixing experiments by varying the percentage of WT versus E-cad  
281 KO cells, (30/70 and 70/30, respectively; Figure 6a and Supplementary Figure 10d,e). In the  
282 latter case, we could even observe E-cad KO colonies surrounded by WT cells which could not  
283 be simply explained by the differential adhesion hypothesis and was not observed in previous  
284 adhesion based studies governed by cortical/line tension [37, 39–43]. We were able to replicate  
285 this in our simulations (Figure 6b). Moreover, to further test the unmixing phase we thought to  
286 probe the unmixing of two cell types with and without E-cadherin, but both showing extensile  
287 behaviour. Since 20  $\mu$ M blebbistatin was shown to reverse the contractile behaviour of E-  
288 cad KO monolayers from contractile to extensile (Supplementary Table 1 and Supplementary  
289 Figure 7), we treated a mixture of WT and E-cad KO plated at 50/50 ratio with blebbistatin after  
290 unmixing. Upon blebbistatin treatment, we see a drop in the mixing index (Figure 6c, Video 5).  
291 In addition, the clear boundaries formed in an untreated sample were lost characterized by the  
292 loss of circularity of WT colonies upon blebbistatin treatment (Figure 6c).

293 Taken together, these results reinforce the fundamental distinctions between phase separation  
294 in systems with differences in activity in comparison to well-established differential line ten-  
295 sion or differential adhesion mechanisms. Even though tissue segregation was first exemplified  
296 based on differences in cadherin-mediated surface tension [37, 38, 42], it was later shown that  
297 intercellular adhesion is not the only mechanism that triggers cell sorting [44]. Theoretical pre-  
298 dictions have suggested that cell sorting could be driven by a combination of cell surface tension  
299 and contractility [39, 40]. While, we cannot completely rule out the contribution of differential

300 adhesion or differential line tension towards the sorting between WT and E-cad KO cells, our  
301 results clearly demonstrate the importance of cell-substrate interaction and intracellular stresses  
302 as key regulators of cell sorting in cellular monolayers with strong adhesion to substrate.

303 The results presented in this work show that epithelial cells are able to maintain their collec-  
304 tive behaviour through a coordination of intercellular and intracellular stresses. Intercellular  
305 stresses are mediated through adherens junctions, while intracellular stresses could be medi-  
306 ated through changes in substrate interaction and actomyosin machinery. Using a combination  
307 of in-silico modelling and extensive experimental studies we have shown that perturbation of  
308 E-cadherin in MDCK cells, increases their substrate interaction in addition to changing their  
309 active nematic behaviour from extensile (WT) to contractile (E-cad KO) similar to a monolayer  
310 of fibroblast which behaves as a contractile unit. Our experimental results also show that per-  
311 turbation of adherens junctions are accompanied by molecular level changes, including reduced  
312 levels of vinculin at cell-cell contacts, together with an increase in focal adhesion size and area  
313 in the absence of E-cadherin, and increase in the number of actin stress fibers on the basal layer.  
314 While, using our numerical model we were able to study how varying inter and intracellular  
315 stresses impacts the active behaviour of cells. In addition, mixing the two different systems  
316 revealed that these differences in active behaviour were sufficient to drive sorting of these do-  
317 mains into an unmixed phase over time. Comparing our observations of sorting with previously  
318 observed studies and hypothesis [37–39] highlights fundamental distinctions that arise due to  
319 the difference in the nature of active forces. These observations bring in a new understand-  
320 ing to the existing models of differential adhesion. Having understood the role of extensility  
321 and contractility in dictating demixing (sorting) of cells, this approach could be expanded to  
322 studying other biological processes such as tissue growth, development and tissue homeosta-  
323 sis. For instance, recent studies demonstrated the importance of nematic organization of actin  
324 cytoskeleton in Hydra during morphogenesis [45], while other studies have begun to explore

325 the role of liquid-crystal ordering during morphogenesis [46] and *in – vivo* epithelial tissue  
326 patterning [47]. These findings highlight the importance of active nematic behaviours at a col-  
327 lective level to understand tissue shape and organization, factors central to morphogenesis [45,  
328 46, 48–50]. As such, the adaptation of cellular systems from extensile to contractile behaviours  
329 might be a crucial mechanism by which a collective living system undergoes morphological  
330 changes (sorting or tissue organization) based on a transition from a cohesive to a less coordi-  
331 nated organization. Such a transition relying on the cross-talk between cell-cell and cell-matrix  
332 interactions may provide a new mechanism to understand cell migration during development,  
333 wound healing, and collective cancer cell invasion.

## 334 **Acknowledgements**

335 This work was supported by the European Research Council (Grant No. CoG-617233), LABEX  
336 Who Am I? (ANR-11-LABX-0071), the Ligue Contre le Cancer (Equipe labellisée), and the  
337 Agence Nationale de la Recherche (‘POLCAM’ (ANR-17-CE13-0013 and ‘MechanoAdipo’  
338 ANR-17-CE13-0012). We acknowledge the ImagoSeine core facility of the IJM, member of  
339 IBiSA and France-BioImaging (ANR-10-INBS-04) infrastructures. A. D. acknowledges sup-  
340 port from the Novo Nordisk Foundation (grant No. NNF18SA0035142), Villum Fonden (Grant  
341 no. 29476), and funding from the European Union’s Horizon 2020 research and innovation pro-  
342 gram under the MarieSkłodowska-Curie grant agreement No. 847523 (INTERACTIONS). LB  
343 has received funding from the European Union’s Horizon 2020 research and innovation pro-  
344 gramme (Marie Skłodowska-Curie grant agreement 665850-INSPIRE). T.B.S. acknowledges  
345 support from the Lee Kuan Yew (LKY) Postdoctoral fellowship and Singapore Ministry of Ed-  
346 ucation Academic Research Fund Tier 1 (R-397-000-320-114). S.G and A. Y were supported  
347 by project grants and fellowships from the National Health and Medical Research Council of  
348 Australia (1123816 and 1139592) and Australian Research Council (DP190102871). We would

349 like to thank Phillipe Marcq for help with implementation of BISM code, Marina A. Glukhova  
350 for providing the vinculin antibody and Sylvie Robine for the ZO1 antibody. AD and JMY  
351 acknowledge Guanming Zhang for helpful discussions regarding the model. We also thank the  
352 members of cell adhesion and mechanics team at Institut Jacques Monod, Matthieu Piel and  
353 Francois Gallet for insightful discussions.

## 354 **Author contributions**

355 L.B, T.B.S, A.D, J.Y, R.M.M and B.L designed the research. G.H.N.S.N and T.D developed the  
356 E-cadherin KO cell line. L.B performed experiments and analysed the results. S.S helped in the  
357 PA gel experiments. M.T performed and quantified laser ablation experiments. S.G performed  
358 the MCF10A experiments. A.D, R.M, performed the in silico simulations. T.B.S contributed to  
359 the analysis tools. A.S.Y, Y.T, R.M.M, A.D, J.Y, and B.L supervised the project.

## 360 **Competing Financial Interests**

361 The authors declare no competing interests.

## 362 **Data availability statement**

363 Source data and codes for cell orientation detection, and Bayesian inference of tissue stress  
364 are available upon request. Numerical analyses were performed using a custom made code  
365 "CELADRO: Cells as Active Droplets", which is an open source code that has been deposited  
366 on GitHub (<https://github.com/rhomu/celadro>).

## Materials and Correspondence

Correspondence and requests for materials should be addressed to A.D (doostmohammadi@nbi.ku.dk), R.M.M (rene-marc.mege@ijm.fr), J.Y (julia.yeomans@physics.ox.ac.uk) and B.L (benoit.ladoux@ijm.fr)

## References

- [1] E. H. Barriga et al. “Tissue Stiffening Coordinates Morphogenesis by Triggering Collective Cell Migration in vivo”. en. In: Nature 554.7693 (Feb. 2018), pp. 523–527. DOI: 10.1038/nature25742.
- [2] T. Onodera et al. “Btbd7 Regulates Epithelial Cell Dynamics and Branching Morphogenesis”. en. In: Science 329.5991 (July 2010), pp. 562–565. DOI: 10.1126/science.1191880.
- [3] X. L. Chen et al. “VEGF-Induced Vascular Permeability Is Mediated by FAK”. en. In: Developmental Cell 22.1 (Jan. 2012), pp. 146–157. DOI: 10.1016/j.devcel.2011.11.002.
- [4] C. Malinverno et al. “Endocytic Reawakening of Motility in Jammed Epithelia”. en. In: Nature Materials 16.5 (May 2017), pp. 587–596. DOI: 10.1038/nmat4848.
- [5] M. Cetera et al. “Epithelial Rotation Promotes the Global Alignment of Contractile Actin Bundles during Drosophila Egg Chamber Elongation”. en. In: Nature Communications 5 (Nov. 2014), p. 5511. DOI: 10.1038/ncomms6511.
- [6] S. Wang, K. Matsumoto, and K. M. Yamada. “Reconstituting Stratified Epithelial Branching Morphogenesis by Engineering Cell Adhesion”. en. In: bioRxiv (June 2020). Publisher: Cold Spring Harbor Laboratory Section: New Results, p. 2020.06.24.165795. DOI: 10.1101/2020.06.24.165795.
- [7] C. De Pascalis and S. Etienne-Manneville. “Single and Collective Cell Migration: The Mechanics of Adhesions”. en. In: Molecular Biology of the Cell 28.14 (July 2017). Ed. by V. M. Weaver, pp. 1833–1846. DOI: 10.1091/mbc.e17-03-0134.
- [8] U. S. Schwarz and S. A. Safran. “Elastic Interactions of Cells”. In: Physical Review Letters 88.4 (Jan. 2002), p. 048102. DOI: 10.1103/PhysRevLett.88.048102.
- [9] G. Duclos et al. “Topological Defects in Confined Populations of Spindle-Shaped Cells”. In: Nature Physics 13 (Jan. 2017), pp. 58–62. DOI: 10.1038/nphys3876.
- [10] T. B. Saw et al. “Topological Defects in Epithelia Govern Cell Death and Extrusion”. en. In: Nature 544.7649 (Apr. 2017), pp. 212–216. DOI: 10.1038/nature21718.
- [11] C. Blanch-Mercader et al. “Turbulent Dynamics of Epithelial Cell Cultures”. en. In: Physical Review Letters 120.20 (May 2018), p. 208101. DOI: 10.1103/PhysRevLett.120.208101.

- 401 [12] K. Kawaguchi, R. Kageyama, and M. Sano. “Topological Defects Control Collective  
402 Dynamics in Neural Progenitor Cell Cultures”. eng. In: Nature 545.7654 (Apr. 2017),  
403 pp. 327–331. DOI: 10.1038/nature22321.
- 404 [13] W. Xi et al. “Material Approaches to Active Tissue Mechanics”. en. In: Nature Reviews Materials  
405 4.1 (Jan. 2019), pp. 23–44. DOI: 10.1038/s41578-018-0066-z.
- 406 [14] H. Gruler, U. Dewald, and M. Eberhardt. “Nematic Liquid Crystals Formed by Living  
407 Amoeboid Cells”. en. In: The European Physical Journal B 11 (1999), p. 6.
- 408 [15] B. Ladoux and R.-M. Mège. “Mechanobiology of Collective Cell Behaviours”. en. In:  
409 Nature Reviews Molecular Cell Biology 18.12 (Dec. 2017), pp. 743–757. DOI: 10.1038/  
410 nrm.2017.98.
- 411 [16] L. Giomi et al. “Defect dynamics in active nematics”. In: Philosophical Transactions of the Royal Society  
412 372.2029 (2014), p. 20130365.
- 413 [17] A. Doostmohammadi et al. “Active nematics”. In: Nature communications 9.1 (2018),  
414 pp. 1–13.
- 415 [18] W. Marth and A. Voigt. “Signaling Networks and Cell Motility: A Computational Ap-  
416 proach Using a Phase Field Description”. en. In: Journal of Mathematical Biology 69.1  
417 (July 2014), pp. 91–112. DOI: 10.1007/s00285-013-0704-4.
- 418 [19] R. Mueller, J. M. Yeomans, and A. Doostmohammadi. “Emergence of Active Nematic  
419 Behavior in Monolayers of Isotropic Cells”. en. In: Physical Review Letters 122.4 (Feb.  
420 2019), p. 048004. DOI: 10.1103/PhysRevLett.122.048004.
- 421 [20] M. R. Ng et al. “Mapping the Dynamics of Force Transduction at Cell–Cell Junctions of  
422 Epithelial Clusters”. In: eLife 3 (Dec. 2014). Ed. by E. Paluch, e03282. DOI: 10.7554/  
423 eLife.03282.
- 424 [21] V. Nier et al. “Inference of Internal Stress in a Cell Monolayer”. In: Biophysical Journal  
425 110.7 (Apr. 2016), pp. 1625–1635. DOI: 10.1016/j.bpj.2016.03.002.
- 426 [22] L. Petitjean et al. “Velocity Fields in a Collectively Migrating Epithelium”. en. In: Biophysical Journal  
427 98.9 (May 2010), pp. 1790–1800. DOI: 10.1016/j.bpj.2010.01.030.
- 428 [23] S. Garcia et al. “Physics of active jamming during collective cellular motion in a mono-  
429 layer”. en. In: Proceedings of the National Academy of Sciences 112.50 (Dec. 2015). Pub-  
430 lisher: National Academy of Sciences Section: Physical Sciences, pp. 15314–15319. DOI:  
431 10.1073/pnas.1510973112.
- 432 [24] K. Goodwin et al. “Cell–cell and cell–extracellular matrix adhesions cooperate to orga-  
433 nize actomyosin networks and maintain force transmission during dorsal closure”. In:  
434 Molecular Biology of the Cell 28.10 (Mar. 2017). Publisher: American Society for Cell  
435 Biology (mboc), pp. 1301–1310. DOI: 10.1091/mbc.e17-01-0033.
- 436 [25] S. Dupont et al. “Role of YAP/TAZ in Mechanotransduction”. eng. In: Nature 474.7350  
437 (June 2011), pp. 179–183. DOI: 10.1038/nature10137.
- 438 [26] G. Giannone et al. “Periodic Lamellipodial Contractions Correlate with Rearward Actin  
439 Waves”. en. In: Cell 116.3 (Feb. 2004), pp. 431–443. DOI: 10.1016/S0092-8674(04)  
440 00058-3.

- 441 [27] A. Zemel et al. “Optimal Matrix Rigidity for Stress-Fibre Polarization in Stem Cells”.  
 442 en. In: Nature Physics 6.6 (June 2010), pp. 468–473. DOI: 10.1038/nphys1613.
- 443 [28] M. Gupta et al. “Adaptive Rheology and Ordering of Cell Cytoskeleton Govern Matrix  
 444 Rigidity Sensing”. en. In: Nature Communications 6.1 (Nov. 2015), p. 7525. DOI: 10.  
 445 1038/ncomms8525.
- 446 [29] A. Saraswathibhatla and J. Notbohm. “Traction and Stress Fibers Control Cell Shape  
 447 and Rearrangements in Collective Cell Migration”. en. In: Physical Review X 10.1 (Jan.  
 448 2020), p. 011016. DOI: 10.1103/PhysRevX.10.011016.
- 449 [30] D. Riveline et al. “Focal Contacts as Mechanosensors”. In: The Journal of Cell Biology  
 450 153.6 (2001), pp. 1175–1186. DOI: 10.1083/jcb.153.6.1175. eprint: [http :  
 451 //jcb.rupress.org/content/153/6/1175.full.pdf](http://jcb.rupress.org/content/153/6/1175.full.pdf).
- 452 [31] S. Yonemura et al. “Alpha-Catenin as a Tension Transducer That Induces Adherens Junc-  
 453 tion Development”. eng. In: Nature Cell Biology 12.6 (June 2010), pp. 533–542. DOI:  
 454 10.1038/ncb2055.
- 455 [32] J. L. Bays and K. A. DeMali. “Vinculin in Cell–Cell and Cell–Matrix Adhesions”. In:  
 456 Cellular and Molecular Life Sciences 74.16 (2017), pp. 2999–3009. DOI: 10.1007/  
 457 s00018-017-2511-3.
- 458 [33] G. Halder, S. Dupont, and S. Piccolo. “Transduction of Mechanical and Cytoskeletal  
 459 Cues by YAP and TAZ”. en. In: Nature Reviews Molecular Cell Biology 13.9 (Sept.  
 460 2012), pp. 591–600. DOI: 10.1038/nrm3416.
- 461 [34] B. W. Benham-Pyle, B. L. Pruitt, and W. J. Nelson. “Mechanical Strain Induces E-  
 462 Cadherin-Dependent Yap1 and  $\beta$ -Catenin Activation to Drive Cell Cycle Entry”. In:  
 463 Science (New York, N.Y.) 348.6238 (May 2015), pp. 1024–1027. DOI: 10.1126/science.  
 464 aaa4559.
- 465 [35] N.-G. Kim et al. “E-Cadherin Mediates Contact Inhibition of Proliferation through Hippo  
 466 Signaling-Pathway Components”. en. In: Proceedings of the National Academy of Sciences  
 467 108.29 (July 2011), pp. 11930–11935. DOI: 10.1073/pnas.1103345108.
- 468 [36] D. E. Discher, P. Janmey, and Y.-l. Wang. “Tissue Cells Feel and Respond to the Stiff-  
 469 ness of Their Substrate”. In: Science 310.5751 (2005), pp. 1139–1143. DOI: 10.1126/  
 470 science.1116995. eprint: [https://science.sciencemag.org/content/  
 471 310/5751/1139.full.pdf](https://science.sciencemag.org/content/310/5751/1139.full.pdf).
- 472 [37] J.-L. Maître et al. “Adhesion Functions in Cell Sorting by Mechanically Coupling the  
 473 Cortices of Adhering Cells”. en. In: Science 338.6104 (Oct. 2012), pp. 253–256. DOI:  
 474 10.1126/science.1225399.
- 475 [38] M. S. Steinberg. “Does differential adhesion govern self-assembly processes in histo-  
 476 genesis? Equilibrium configurations and the emergence of a hierarchy among popula-  
 477 tions of embryonic cells”. en. In: Journal of Experimental Zoology 173.4 (1970). eprint:  
 478 <https://onlinelibrary.wiley.com/doi/pdf/10.1002/jez.1401730406>, pp. 395–433. DOI: 10.  
 479 1002/jez.1401730406.
- 480 [39] M. L. Manning et al. “Coaction of intercellular adhesion and cortical tension speci-  
 481 fies tissue surface tension”. In: Proceedings of the National Academy of Sciences 107.28

- 482 (2010), pp. 12517–12522. DOI: 10.1073/pnas.1003743107. eprint: <https://www.pnas.org/content/107/28/12517.full.pdf>.
- 483
- 484 [40] P. Sahu et al. “Small-scale demixing in confluent biological tissues”. en. In: Soft Matter  
485 16.13 (Apr. 2020). Publisher: The Royal Society of Chemistry, pp. 3325–3337. DOI:  
486 10.1039/C9SM01084J.
- 487 [41] M. Krajnc. “Solid–fluid transition and cell sorting in epithelia with junctional tension  
488 fluctuations”. en. In: Soft Matter 16.13 (Apr. 2020). Publisher: The Royal Society of  
489 Chemistry, pp. 3209–3215. DOI: 10.1039/C9SM02310K.
- 490 [42] W. A. Thomas et al. “Two distinct adhesion mechanisms in embryonic neural retina cells:  
491 III. Functional specificity”. In: Developmental Biology 81.2 (1981), pp. 379–385. DOI:  
492 [https://doi.org/10.1016/0012-1606\(81\)90304-3](https://doi.org/10.1016/0012-1606(81)90304-3).
- 493 [43] R. A. Foty and M. S. Steinberg. “Cadherin-mediated cell-cell adhesion and tissue segre-  
494 gation in relation to malignancy”. eng. In: The International Journal of Developmental Biology  
495 48.5-6 (2004), pp. 397–409. DOI: 10.1387/ijdb.041810rf.
- 496 [44] C. M. Niessen and B. M. Gumbiner. “Cadherin-mediated cell sorting not determined by  
497 binding or adhesion specificity”. In: The Journal of Cell Biology 156.2 (2002), pp. 389–  
498 400. DOI: 10.1083/jcb.200108040. eprint: [http://jcb.rupress.org/  
499 content/156/2/389.full.pdf](http://jcb.rupress.org/content/156/2/389.full.pdf).
- 500 [45] Y. Maroudas-Sacks et al. “Topological defects in the nematic order of actin fibers as orga-  
501 nization centers of Hydra morphogenesis”. en. Publisher: Cold Spring Harbor Laboratory  
502 Section: New Results. Mar. 2020. DOI: 10.1101/2020.03.02.972539.
- 503 [46] J. Comelles et al. “Epithelial colonies in vitro elongate through collective effects”. en.  
504 Publisher: Cold Spring Harbor Laboratory Section: New Results. Apr. 2020. DOI: 10.  
505 1101/755181.
- 506 [47] H. Morales-Navarrete et al. “Liquid-crystal organization of liver tissue”. In: eLife 8 (June  
507 2019). Ed. by P. Sens, A. K. Chakraborty, and B. Ladoux, e44860. DOI: 10.7554/  
508 eLife.44860.
- 509 [48] B. Aigouy et al. “Cell Flow Reorients the Axis of Planar Polarity in the Wing Epithelium  
510 of Drosophila”. In: Cell 142.5 (2010), pp. 773–786. DOI: [https://doi.org/10.  
511 1016/j.cell.2010.07.042](https://doi.org/10.1016/j.cell.2010.07.042).
- 512 [49] E. Hannezo, J. Prost, and J.-F. Joanny. “Theory of Epithelial Sheet Morphology in Three  
513 Dimensions”. en. In: Proceedings of the National Academy of Sciences 111.1 (Jan. 2014),  
514 pp. 27–32. DOI: 10.1073/pnas.1312076111.
- 515 [50] H. Morales-Navarrete et al. “Liquid-crystal organization of liver tissue”. In: eLife 8 (June  
516 2019). Ed. by P. Sens, A. K. Chakraborty, and B. Ladoux. Publisher: eLife Sciences  
517 Publications, Ltd, e44860. DOI: 10.7554/eLife.44860.

## 518 **Methods**

519 **Cell culture and reagents** MDCK WT (ATCC CCL-34) cells, MCF7A cells (ATCC HTB-  
520 22), MDCK E-cadherin Knock-Out (KO) cells and shMCF7A E-cadherin KD cells were cul-  
521 tured in DMEM (containing Glutamax, High Glucose, and Pyruvate, Life Technologies) supple-  
522 mented with 10% foetal bovine serum (Life Technologies) and 1% penicillin-streptomycin (Life  
523 Technologies) at 37°C with 5% CO<sub>2</sub>. For cell migration experiments, cells were left to spread  
524 overnight before imaging so that the cells form a complete monolayer. Prior to imaging, normal  
525 culture media (DMEM) was changed to low glucose DMEM (containing Pyruvate, Life Tech-  
526 nologies) in order to minimize cell division as cell divisions were known to generate extensile  
527 flow [51]. In our coculture mixing experiments, in order to ensure we have a mixed population at  
528 the start of imaging, cells were plated with low Ca<sup>2+</sup> media (no FBS) for 3 hours, and changed  
529 to normal media once the cells attach. For immunofluorescent stainings, cells were fixed with  
530 4% paraformaldehyde (PFA), permeabilized with 0.5% Triton-X 100 for 5 minutes, blocked  
531 with 1% BSA/PBS for 1 hour, and incubated with primary antibody overnight at 4°C. The  
532 samples were then incubated with secondary antibody and Hoescht (Thermo Fisher)(1:10000)  
533 for 1 hour and mounted on Mowiol 4-88 (Sigma Aldrich C2081) before imaging. The pri-  
534 mary antibodies used were directed against E-cadherin (24E10- Cell Signaling Technology;  
535 DECMA1- Sigma Aldrich) (1:100), cadherin 6(1:50) [52], paxillin (Y133- Abcam) (1:100),  
536 pMLC2 (Cell Signaling) (1:100), vinculin (kindly provided by Marina Glukhova) (1:2) [53],  
537  $\alpha$ -catenin (Sigma Aldrich)(1:100),  $\beta$ -catenin (BD Biosciences) (1:100), ZO1 (a generous gift  
538 from Sylvie Robin) (1:50), YAP (Santa Cruz Biotechnology) (1:100). Anti-mouse, anti-rat, and  
539 anti-rabbit secondary antibodies conjugated with Alexa (488 or 568)(used at 1:200 dilution),  
540 Alexa 647 (1:50) conjugated phalloidin were purchased from Life Technologies. A slightly  
541 different fixation protocol was used to stain vinculin at the cell-cell junction and focal adhe-

542 sion sites. In order to label vinculin at cell-cell contact sites, cells were fixed with a mix of  
543 4% PFA and 0.5% Triton-X 100 for 1 minute 30 seconds, followed by fixation with 4% PFA  
544 for 10 minutes. While staining for vinculin at focal adhesion sites, cells were fixed with 4%  
545 PFA for 10 minutes, followed by permeabilization with 0.5% Triton-X 100 for 10minutes. For  
546 experiments requiring inhibition of contractility blebbistatin 5  $\mu$ M, 20  $\mu$ M (Sigma Aldrich) or  
547 Y27632 25  $\mu$ M (Sigma Aldrich) were added just before imaging.

548 **Generation of E-cadherin KO cell line** MDCK E-cadherin KO stable cells were gener-  
549 ated using a CRISPR-Cas9 double nickase plasmid (Santa Cruz Biotechnology). The follow-  
550 ing gRNA sequences were used: TGATGACACCCGATTCAAAG and ATAGGCTGTCCTAG-  
551 GTAGAC. Around 2 million cells were electroporated (Neon Transfection System Invitrogen)  
552 with 3 $\mu$ g of plasmid in one pulse of 20 ms and at 1650V. Twenty four hours later, cells were  
553 selected by adding 2.5  $\mu$ g/ml puromycin in the culture media. Fourty eight hours later, GFP  
554 positive single cells were sorted in 96 well plates by flow cytometry using Influx 500 sorter-  
555 analyzer (BD BioSciences). The clonal populations were then selected based on the absence of  
556 E-cadherin by immunofluorescence staining. The absence of E-cadherin in the clones generated  
557 was confirmed by Western blot analysis of protein extracts (Extended Figure 2b).

558 **Generation of siRNA E-cadherin KD cells** Lipofectamine RNAiMAX (Invitrogen) was  
559 used for siRNA transfection. siRNA sequences were control (on-target plus nontargeting pool),  
560 UGGUUUACAUGUCGACUAA. siRNA against E-cadherin : GGGACAACGUUUAUUACUA  
561 was used. The levels of E-cadherin was confirmed by Western blot analysis of protein extracts  
562 (Extended Figure 3a).

563 **Live cell and fixed sample imaging** Live imaging was performed with a 10X objective on  
564 BioStation IM-Q (Nikon) at 37°C and 5% CO<sub>2</sub>. Images are acquired every 10 min. For mi-

565 gration experiments, just the phase contrast images were captured every 10 min. For TFM  
566 experiments, phase contrast and fluorescent beads were imaged.

567 **Calculation of cell area, aspect ratio and molecular markers** The cellular area and aspect  
568 ratio were obtained from time lapse imaging of phase contrast images. Cells were then seg-  
569 mented using MorphoLibJ, an ImageJ plugin for cell segmentation. The area and length of  
570 paxillin was obtained by fitting them with an ellipse. Nuclear-cytoplasmic ratio of YAP inten-  
571 sity was quantified using an in-house ImageJ script. If the nucleus-cytoplasmic ratio was greater  
572 than 1.1 then YAP was considered to be nuclear while a value less than 0.99 was considered  
573 to be more cytoplasmic while any value in between was considered to be uniformly distributed  
574 through the cell.

575 **Western Blot** Proteins for MDCK cells were extracted using RIPA buffer without SDS (50mM  
576 Tris pH 7.5, 150mM NaCl, 1% NP40, 5mM EDTA, 1mM Na<sub>3</sub>VO<sub>4</sub>, 10mM NaF, 1mM PMSF,  
577 1X protease inhibitor cocktail (Roche) and 1X phosphatase inhibitor (Phosphostop, Roche).  
578 Proteins from MCF7 cells were extracted using sample buffer (50mM Tris pH 7.5, SDS 2%,  
579 Glycerol 10%, Bromophenol blue 0.1%, Dithiothreitol 400nM, sterile water). Protein concen-  
580 tration was quantified by a Bradford assay (BioRad). 30 µg of protein were loaded onto NuPage  
581 4-12% Bis-Tris gel using a mini gel tank and dry transferred using iBlot transfer system (Invitro-  
582 gen). Non-specific sites were blocked using 5% non fat dry milk in 0.1% PBS Tween. For MLC  
583 total, blots were blocked with BSA/TBST (Tris buffered saline with Tween 20). Primary anti-  
584 bodies were diluted in PBS Tween at E-cadherin (24E10- 1:1000 for MDCK cells) (Santa Cruz,  
585 SC7870- 1:200 for MCF7 cells),  $\alpha$ -catenin (1:1000),  $\beta$ -catenin (1:1000), vinculin (gift from  
586 Marina Glukhova, 1:500), GAPDH (Protein Tech Europe 60004-1 for MDCK cells and abcam-  
587 1:5000, ab181603 for MCF7 cells- 1:500), alpha-tubulin (1:5000) (Sigma T9026) overnight on  
588 a shaker at 4 °C. Anti-MLC (Cell Signaling) antibodies were diluted in TBST. The blots were

589 then washed 3-4 times for 10 minutes each in PBS 0.1% Tween or TBST (for pMLC2 and MLC  
590 total antibodies). They were then incubated with either Gambox, HRP linked (Sigma Aldrich,  
591 Pierce or Santa Cruz) or Dylight 800 linked secondary antibodies (ThermoFisher Scientific) for  
592 2 hours. The blots were then washed three times with PBS 0.1% Tween or TBST for 10 minutes  
593 each. The blots were then revealed using CHEMIDOC MP (BioRad) using Super West Femto  
594 (34095 Thermo Scientific) or chemiluminescence.

595 **Traction force microscopy** Soft silicone substrates were prepared as described previously  
596 [54]. CyA and CyB were mixed in the ratio 1:1 and directly poured on glass bottom Petri  
597 dishes (fluorodish) in order to obtain a 100  $\mu\text{m}$  thick layer. The substrate was cured at room  
598 temperature overnight on a flat surface. To ensure complete curing, the samples were cured at  
599 80°C for 1 hour the next day. The surface was silanized using a solution of 5% APTES diluted  
600 in absolute ethanol for 5 min. The substrate was then washed with absolute ethanol and dried at  
601 80°C for 10 min. 200 nm carboxylated fluorescent beads (Invitrogen) were diluted in deionized  
602 water solution at 1:500 for 10 min, washed with deionized water and dried at 80°C for 10 min.  
603 We then coated these substrates with 50  $\mu\text{g}/\text{ml}$  fibronectin for 1 hour and washed with PBS prior  
604 to cell seeding. Around 200,000 cells were seeded in each petridish 40-50 min and washed with  
605 media when enough cells have attached. The cells were let to attach and spread overnight.  
606 The cells are imaged for 24 hours and at the end of the experiment, cells were removed with  
607 the addition of 500  $\mu\text{L}$  of 10% SDS in the media so that the resting position of beads can be  
608 obtained.

609 **Laser ablation** The apical section of the cell which showed the highest Lifeact-Ruby intensity  
610 was used for junctional ablation. This experiment was performed using the ultraviolet laser  
611 ablation system (355nm, 300ps pulse duration, 1 kHz repetition rate, PowerChip PNV-0150-  
612 100, team photonics) [55]. Junctions between two tricellular contacts were ablated using the

613 following parameters: laser power - 120nW, exposure time - 0.3sec and imaging interval -  
614 2.2sec. Recoil velocity was computed by i) calculating the internodal distance after ablation by  
615 tracking the cartesian coordinates of the tricellular junctional nodes using MTrackJ plugin in  
616 Fiji [56] ii) fitting the calculated internodal distance into a single/double exponential function  
617 iii) obtaining recoil velocity using derivative of the function through a custom-made MATLAB  
618 algorithm [55]. The length of the junction was measured by drawing a line ROI in Fiji [57].  
619 Junctional length and associated recoil velocity were plotted.

620 **Soft polyacrylamide gel patterning** Glass coverslips were plasma activated and coated with  
621 0.1mg/ml PLL-g-PEG (SuSoS Technology). 1mm diameter circles were patterned on the pas-  
622 sivated glass coverslips using deep UV and incubated the glass coverslips with 20  $\mu$ g/ml fi-  
623 bronectin for 30 minutes. After incubation, glass coverslips were rinsed in 1x PBS to remove  
624 excess protein. Simultaneously, silanization of another set of glass coverslips were performed  
625 by plasma activation of clean coverslips followed by incubation with an ethanol solution con-  
626 taining 2% (v/v) 3-(trimethoxysilyl) propyl methacrylate (Sigma-Aldrich, St Louis, Missouri,  
627 USA) and 1% (v/v) acetic acid. The silanised coverslips were heated at 120°C. Freshly made  
628 polyacrylamide (PA) mix (7.5% acrylamide, 0.075% bis-acrylamide, 0.05% ammonium persul-  
629 phate and 0.75  $\mu$ l TEMED) was sandwiched between the patterned glass coverslip and silanized  
630 coverslip. The acrylamide, bis-acrylamide concentration was the same as [58], to generate 2.3  
631 kPa PA gels. After polymerization, the patterned coverslips were peeled off to reveal the pat-  
632 terns of protein on PA gels. Samples were kept submerged in 1x PBS until cell seeding.

633 **Analysis methods** Nematic analysis: Orientation field and defects were detected as described  
634 previously [10]. In short, the largest eigenvector of the structure tensor was obtained for each  
635 pixel while the orientation of cells were obtained using a plugin on ImageJ called OrientationJ.  
636 Using the winding number parameter, we identify defects within the monolayer. Then we obtain

637 the local nematic order parameter tensor  $Q$  (which is averaged over a region of 3-4 cells). The  
638 largest eigenvector of  $Q$  was taken to be the orientation of 3-5 cells and plotted as red lines over  
639 the phase image to ensure that orientation identified is correct. Using this  $Q$  value automated  
640 defect detection can be done using the winding number parameter thereby detecting the various  
641 defects (+1/2, -1/2, +1 and -1) although we have more +1/2 or -1/2 defects. In order to reduce  
642 noise, only stable defects which are found in at least six consecutive frames (60 mins) are used  
643 in the following analysis as described in [10]. In addition, we manually tracked a few defects  
644 over time to verify their movement direction.

645 Velocity analysis: We use PIVlab (a tool implemented using Matlab) to analyse the veloc-  
646 ity of cellular monolayers. An interrogation window of 64x64 (40.96  $\mu\text{m}$ ) and 32x32 pixels  
647 (20.48  $\mu\text{m}$ ) with an overlap of 50% were used for this analysis. Outlier vectors were manually  
648 removed and a local standard deviation filter was applied. The velocity correlation length was  
649 obtained using the formula as detailed in [22].

650 Strain rate and stress measurement: Having identified the location of defects, we obtain the  
651 velocity field around the defects identified by aligning these defects. The strain rate was cal-  
652 culated from the gradient of the velocity field as  $\dot{\epsilon} = \nabla \mathbf{v}$ . By plotting the strain rate and  
653 velocity around the defect, we can characterize the system as an extensile or contractile system.  
654 For force measurement, the beads images obtained during cell migration are merged with the  
655 reference bead images obtained after SDS treatment. The images are stabilized using the Im-  
656 age Stabilizer plugin in ImageJ after which the illumination is corrected to remove background  
657 noise. We then obtain the displacement of beads using PIV of interrogation window 32x32  
658 pixel with an overlap of 50%. Using the ImageJ plugin FTTC [59] we correlate the bead dis-  
659 placement to traction forces using a regularization parameter of  $9 \times 10^{-9}$ . Stress within the  
660 monolayer was estimated using Bayesian Inversion Stress Microscopy (BISM) with a regulari-

661 sation parameter of  $\Lambda = 10^{-6}$  [21]. This method obtains the stress directly from traction forces  
 662 irrespective of epithelial rheology. Isotropic stress was obtained as half the trace of the stress  
 663 tensor  $((s_{xx} + s_{yy})/2)$  in the tissue. Since the stress values obtained through this method are  
 664 not reliable very close to the boundary, only defects in the center of the monolayer have been  
 665 taken into account in these calculations. The heatmaps obtained for strain rate and stress were  
 666 smoothed through linear interpolation.

667 **Statistics** Differences between data were assessed using unpaired t-test implemented in Mat-  
 668 lab and further verified using Graphpad Prism. On the plots, n.s.: not significant,  $*p < 0.05$ ,  
 669  $**p < 0.01$ ,  $***p < 0.001$  and  $****p < 0.0001$ .

670 **Computational model** The model used in this manuscript is the extension of a recently de-  
 671 veloped phase-field model that has been shown to reproduce active nematic behavior in cellular  
 672 tissues [19] and has been quantitatively compared with experiments showing coherent oscilla-  
 673 tions in confined epithelial monolayers [60]. We consider a two-dimensional tissue and describe  
 674 each cell  $i$  independently by a phase-field  $\phi_i$ , where  $\phi_i \simeq 1$  indicates the interior of the cell and  
 675  $\phi_i \simeq 0$  its exterior. The interface of each cell thus lies at  $\phi_i = 1/2$ . The phase-field dynamics is  
 676 given by a Cahn-Allen type evolution equation:

$$\partial_t \phi_i + \mathbf{v}_i \cdot \nabla \phi_i = -\frac{\delta \mathcal{F}}{\delta \phi_i}, \quad (1)$$

where  $\mathbf{v}_i$  is the cell velocity that is determined from an over-damped equation for force balance as detailed below.  $\mathcal{F}$  is the free energy that determines both mechanical properties of the cell - including cell stiffness and compressibility - and details of the passive interactions between the cells. As such the free energy  $\mathcal{F} = \mathcal{F}_{\text{G-L}} + \mathcal{F}_{\text{area}} + \mathcal{F}_{\text{rep}}$  is composed of (i) Ginsburg-Landau term  $\mathcal{F}_{\text{G-L}}$ , that stabilises the interface, (ii) a soft constraint for area conservation  $\mathcal{F}_{\text{area}}$ , that penalises deviations from an initial circular morphology of the cell, and (iii)  $\mathcal{F}_{\text{rep}}$ , which prevents two

phase-fields from overlapping:

$$\begin{aligned}
F_{\text{G-L}} &= \sum_i \int d\mathbf{x} \gamma \left\{ \frac{30}{\lambda^2} \phi_i^2 (1 - \phi_i)^2 + (\nabla \phi_i)^2 \right\}, \\
F_{\text{area}} &= \sum_i \frac{\mu}{\pi R^2} \left( \pi R^2 - \int d\mathbf{x} \phi_i^2 \right)^2, \\
F_{\text{rep}} &= \sum_i \sum_{j \neq i} \frac{30\kappa}{\lambda^2} \int d\mathbf{x} \phi_i^2 \phi_j^2,
\end{aligned}$$

677 where  $\lambda$  sets the interface width,  $\gamma$  sets the stiffness,  $\mu$  determines cells compressibility, and  
678  $\kappa$  sets the strength of repulsion between two phase-fields. For the details of these free energy  
679 definitions, the reader is referred to recent reviews of phase-field models [61, 62] and to [19, 60,  
680 63, 64] for recent implementations. Note that because here we model highly-packed, confluent  
681 tissues we do not introduce any thermodynamic attraction between the cells.

682 **Force balance.** We consider over-damped dynamics of cells moving on a substrate:

$$\xi \mathbf{v}_i = \mathbf{F}_i^{\text{tot}}, \quad (2)$$

683 where  $\xi$  is the friction coefficient between the cells and the substrate, and  $\mathbf{F}_i^{\text{tot}}$  denotes the  
684 total forces acting on each cell. This encompasses self-propulsion forces generated by the cell  
685  $\mathbf{F}_i^{\text{SP}}$  and the interaction forces  $\mathbf{F}_i^{\text{int}}$  that a cell experiences from the neighbouring cells in the  
686 monolayer.

687 The self-propulsion force of an individual cell is achieved through an intricate coordination of  
688 actin polymerisation and myosin contractility. First, actin polymerisation at the cell front results  
689 in the formation of (lamellipodium) protrusions that deform the cell. Myosin contractility then  
690 retracts the cell rear to propel the cell forward. To account for the protrusion effects we introduce  
691 a polarity force  $\alpha \mathbf{p}_i$ , that is distributed over the front edge of the cell in the direction of the cell  
692 polarity  $\mathbf{p}_i$ , where  $\alpha$  sets the strength of the polarity force. To account for the cell contractility,

693 we then introduce a contractile stress  $\zeta_c Q_i$ , where  $\zeta_c$  is the strength of the contractility and  
694  $Q_i = \mathbf{p}_i^T \mathbf{p}_i - \frac{\mathbb{1}}{2} \mathbf{p}_i^2$  is the tensor that characterises the orientation of the polarity: the largest  
695 eigenvector of  $Q_i$  is  $\mathbf{p}_i$  meaning that the contractile stress acts along the direction of protrusions  
696 formation. Considering that the vectors  $\nabla \phi_i$  describe the normal vector to the interface we  
697 obtain the following expression for the self-propulsion force:

$$\mathbf{F}_i^{\text{sp}} = \alpha \mathbf{p}_i + \int d\mathbf{x} \left( \zeta_c \sum_j \phi_j Q_j \right) \nabla \phi_i, \quad (3)$$

698 where matrix multiplication is implied in the last term.

699 Next we consider the interaction stresses  $\sigma_i^{\text{int}}$  to define the interaction forces  $\mathbf{F}_i^{\text{int}} = \int d\mathbf{x} \phi_i \vec{\nabla} \cdot \sigma^{\text{int}} =$   
700  $-\int d\mathbf{x} \sigma^{\text{int}} \cdot \nabla \phi_i$ . Note that  $\vec{\nabla} \phi$  is only non-zero at the interfaces between the cells and as such  
701 the interaction force is acting at the cell-cell interfaces. We decompose the interaction stress  
702 in between the cells into passive and active contributions  $\sigma_i^{\text{int}} = \sigma_i^{\text{passive}} + \sigma_i^{\text{active}}$ : the passive  
703 contribution has a thermodynamic nature and is calculated from the free-energy:

$$\sigma_i^{\text{passive}} = \sum_i -\frac{\delta \mathcal{F}}{\delta \phi_i} \quad (4)$$

704 while the active contribution leads to the force generation between cells at their interface through  
705 adherens junction. Following our recent work [19] this takes the form

$$\sigma_i^{\text{active}} = \zeta_s \sum_j \phi_j S_j, \quad (5)$$

706 where  $S_i = -\int d\mathbf{x} (\vec{\nabla} \phi_i)^T \vec{\nabla} \phi_i$  is the deformation tensor for cell  $i$ , characterising the anisotropy  
707 of the cell shape such that the largest eigenvector of  $S_i$  corresponds to the direction of the  
708 elongation of the cell.

709 **Alignment dynamics.** We now introduce the dynamics of the cell polarity, modeling the  
710 mechanism that determines in which direction the polar force should act. There are many

711 ways to introduce a dynamics of the polarisation [65]. One such way is through modeling the  
712 phenomenon of “contact inhibition of locomotion (CIL)”, aligning the polarity of the cell to the  
713 direction of the total interaction force acting on the cell [66]: We define the dynamics of the  
714 polarisation to be given by

$$\partial_t \theta_i = -J |\mathbf{F}_i^{\text{int}}| \Delta \theta_i + D_r \eta, \quad (6)$$

715 where  $\theta_i \in [-\pi, \pi]$  is the angle that the polarity vector is pointing at – such that  $\mathbf{p}_i = (\cos \theta_i, \sin \theta_i)$   
716 – and  $\eta$  is a Gaussian white noise with zero mean, unit variance, and the rotational diffusivity  
717  $D_r$ . The positive constant  $J$  sets the time scale for the alignment of the polarity to the total  
718 interaction force, as was suggested theoretically [66] and has been recently confirmed in the  
719 experiments on epithelial cells [60]. As explained in [60] this model of alignment has the ad-  
720 vantage that (i) it contains an explicit timescale and (ii) does not require that a cell ‘knows’  
721 about the position of its neighbours.

722 **Simulation details** We simulated equation (1) using a finite difference scheme on a square  
723 lattice with a predictor-corrector step. Throughout this article, we used the following numerical  
724 values for the simulation parameters:  $R = 8$ ,  $\lambda = 3.0$ ,  $\gamma = 0.04$ ,  $\mu = 4.0$ ,  $\kappa = 0.4$ ,  $\xi = 1$ ,  
725  $\alpha = 0.2$ ,  $\zeta_c = 0.08$ , and  $\zeta_s = -0.02$  for the wild type case, while  $\zeta_s = 0.0$  for the case with no  
726 cell-cell interaction stresses. We simulated square domains of edge length  $W = 100, 200, 400$   
727 lattice sites with a packing fraction of  $\Phi = 1.2$  cells and set  $D_r = 1 \times 10^{-3}$  and  $J = 0.1$ .

## 728 **References**

- 729 [51] A. Doostmohammadi et al. “Celebrating Soft Matter’s 10th Anniversary: Cell division:  
730 a source of active stress in cellular monolayers”. In: Soft Matter 11 (37 2015), pp. 7328–  
731 7336. DOI: 10.1039/C5SM01382H.
- 732 [52] V. Marthiens et al. “Complementary Expression and Regulation of Cadherins 6 and 11  
733 during Specific Steps of Motoneuron Differentiation”. In: Molecular and Cellular Neuroscience  
734 20.3 (July 2002), pp. 458–475. DOI: 10.1006/mcne.2002.1130.

- 735 [53] M. A. Glukhova, M. G. Frid, and V. E. Koteliansky. “Developmental changes in ex-  
736 pression of contractile and cytoskeletal proteins in human aortic smooth muscle.” In:  
737 Journal of Biological Chemistry 265.22 (1990), pp. 13042–6. eprint: <http://www.jbc.org/content/265/22/13042.full.pdf+html>.  
738
- 739 [54] S. R. K. Vedula et al. “Epithelial Bridges Maintain Tissue Integrity during Collective  
740 Cell Migration”. en. In: Nature Materials 13.1 (Jan. 2014), pp. 87–96. DOI: 10.1038/  
741 nmat3814.
- 742 [55] Y. Hara, M. Shagirov, and Y. Toyama. “Cell Boundary Elongation by Non-autonomous  
743 Contractility in Cell Oscillation”. English. In: Current Biology 26.17 (Sept. 2016). Pub-  
744 lisher: Elsevier, pp. 2388–2396. DOI: 10.1016/j.cub.2016.07.003.
- 745 [56] E. Meijering, O. Dzyubachyk, and I. Smal. “Methods for cell and particle tracking”. eng.  
746 In: Methods in Enzymology 504 (2012), pp. 183–200. DOI: 10.1016/B978-0-12-  
747 391857-4.00009-4.
- 748 [57] J. Schindelin et al. “Fiji: an open-source platform for biological-image analysis”. In:  
749 Nature Methods 9.7 (July 2012), pp. 676–682. DOI: 10.1038/nmeth.2019.
- 750 [58] S. V. Plotnikov et al. “High-resolution traction force microscopy”. eng. In: Methods in cell biology  
751 123 (2014), pp. 367–394. DOI: 10.1016/B978-0-12-420138-5.00020-3.
- 752 [59] Q. Tseng et al. “Spatial Organization of the Extracellular Matrix Regulates Cell–Cell  
753 Junction Positioning”. en. In: Proceedings of the National Academy of Sciences 109.5  
754 (Jan. 2012), pp. 1506–1511. DOI: 10.1073/pnas.1106377109.
- 755 [60] G. Peyret et al. “Sustained Oscillations of Epithelial Cell Sheets”. In: Biophysical Journal  
756 117.3 (Aug. 2019), pp. 464–478. DOI: 10.1016/j.bpj.2019.06.013.
- 757 [61] I. S. Aronson, ed. Physical Models of Cell Motility. en. Biological and Medical Physics,  
758 Biomedical Engineering. Springer International Publishing, 2016.
- 759 [62] B. A. Camley and W.-J. Rappel. “Physical Models of Collective Cell Motility: From  
760 Cell to Tissue”. eng. In: Journal of Physics D: Applied Physics 50.11 (2017). DOI: 10.  
761 1088/1361-6463/aa56fe.
- 762 [63] B. Palmieri et al. “Multiple Scale Model for Cell Migration in Monolayers: Elastic  
763 Mismatch between Cells Enhances Motility”. eng. In: Scientific Reports 5 (July 2015),  
764 p. 11745. DOI: 10.1038/srep11745.
- 765 [64] B. Winkler, I. S. Aranson, and F. Ziebert. “Confinement and Substrate Topography Con-  
766 trol Cell Migration in a 3D Computational Model”. en. In: Communications Physics 2.1  
767 (July 2019), pp. 1–11. DOI: 10.1038/s42005-019-0185-x.
- 768 [65] R. Alert and X. Trepat. “Physical Models of Collective Cell Migration”. In: Annual Review of Condensed  
769 11.1 (2020), null. DOI: 10.1146/annurev-conmatphys-031218-013516.  
770 eprint: [https://doi.org/10.1146/annurev-conmatphys-031218-](https://doi.org/10.1146/annurev-conmatphys-031218-013516)  
771 [013516](https://doi.org/10.1146/annurev-conmatphys-031218-013516).
- 772 [66] B. Smeets et al. “Emergent Structures and Dynamics of Cell Colonies by Contact Inhi-  
773 bition of Locomotion”. en. In: Proceedings of the National Academy of Sciences 113.51  
774 (Dec. 2016), pp. 14621–14626. DOI: 10.1073/pnas.1521151113.

**Figure 1| Active nematic behaviour of epithelial cellular systems changes from extensile to contractile in the absence of E-cadherin.** a) Top, left and right: typical examples of traction force magnitude maps for a single MDCK WT and E-cadherin KO cell cultured on deformable PDMS surfaces. Bottom, left and right: vectorial maps of traction forces for a single MDCK WT and E-cadherin KO cell on a soft PDMS substrate. Scale bars,  $20\mu\text{m}$ . b) Schematic showing the defect movement based on force balance for an extensile active nematic system (left) and contractile active nematic system (right) with an inset of forces exerted on neighbours by an extensile (left) and contractile (right) nematic particle. c) Schematic (left) and experimental (right) images of  $+1/2$  defect (left, comet configuration) and  $-1/2$  defect (right, trefoil configuration). Scale bars,  $20\mu\text{m}$ . d) Average  $yy$ - and  $xy$  components of strain rate map around  $+1/2$  defect obtained from experiments (left and middle respectively) and corresponding average flow field (right) for MDCK WT cells (top) ( $n = 1934$  defects from 2 independent experiments) and MDCK E-cadherin KO cells (bottom) ( $n = 1,884$  defects from 2 independent experiments). Schematic on the extreme right illustrates the movement of defects. Colour code is positive for stretching and negative for shrinkage. e, f) Experimental data for MDCK WT (e) and MDCK E-cadherin KO (f) monolayers. Top panels: phase contrast images of the cells overlaid with the average local orientation of the cells (red lines). Bottom panels: average local orientation of the cells (red lines). The blue circle shows the location of a  $+1/2$  defect and the corresponding arrow indicates the direction of motion of this defect over time. Dashed lines have been added for better reading of defect movement. Scale bars,  $40\mu\text{m}$ .

**Figure 2| Balance of intercellular and intracellular stresses dictate the extensile and contractile behaviour of a 2D nematic system** a) Schematic illustrating the model used in numerical simulations which incorporates cell-cell interaction through active intercellular forces. The direction of cell elongation is denoted by the headless vector  $\hat{s}$ , which is found from the eigenvector corresponding to the largest eigenvalue of the shape tensor  $\mathbf{S}$  for each cell. b) Numerical simulations for the case without active intercellular stresses, showing: (top), phase contrast images of the cells overlaid with the average local orientation of the cells (red lines) and (bottom), average local orientation of the cells (red lines). The blue circle shows the location of a  $+1/2$  defect and the corresponding arrow indicates the direction of motion of this defect over time. c) Average  $yy$ - and  $xy$ -components of strain rate map around  $+1/2$  defect obtained from simulations (left and middle respectively) and corresponding average velocity flow field (right:  $n = 2,083$  defects) for the control condition (top) and the condition without active intercellular forces. Colour code is positive for stretching and negative for shrinkage. d) RMS velocity, and e) the velocity correlation length in the monolayer normalized to the individual cell size obtained from  $n=30$  different simulations for the control condition and the condition without active intercellular forces.

**Figure 3| Knocking out E-cadherin increases cell-substrate interactions.** a) Average isotropic stress around a  $+1/2$  defect obtained from simulations for the control condition (left) and condition without intercellular forces (right) ( $n = 2,083$  defects). b,c) Average  $yy$  (left)-,  $xy$  (middle)- and isotropic (right) components of stress around a  $+1/2$  defect obtained from experiments for (b) MDCK WT ( $n = 1,899$  defects) and (c) E-cadherin KO ( $n = 1,428$  defects) from 2 independent experiments. For a and b colour code represents the strength of the stress with positive for tensile state, negative for compression. d, e, f) velocity correlation length (d) ( $n=10$ ), velocity (e) ( $n=10$ ) and mean traction force (f) ( $n=12$ ) of cells within a monolayer for both MDCK WT and MDCK E-cadherin KO cells. g, h) Cell spreading area (g) and aspect ratio (h) of cells within the monolayer obtained from  $n=10$  different images for MDCK WT and E-cadherin KO cells as a function of time

from 2 independent experiments. The error bars represent the standard deviation. Unpaired t-test was performed resulting in  $*p<0.05$ ,  $**p<0.01$ ,  $***p<0.001$  and  $****p<0.0001$ .

**Figure 4| E-cadherin removal triggers mechanotransductive changes within the monolayer.**

a) pMRLC (left), zoom of pMRLC (middle), actin (right) staining of MDCK WT (top) and E-cadherin KO (bottom) monolayers. b) Evolution of mean traction force of MDCK WT and E-cadherin KO monolayers before and after 20 $\mu$ M blebbistatin treatment ( $n=10$  from 2 independent experiments). c, d, e) actin (red) and paxillin (green) (c), vinculin (d), YAP (green), and nucleus (blue) (e), staining within a monolayer for both MDCK WT and E-cadherin KO cells. c) Area of focal adhesion (left) and length of focal adhesion within the monolayer for  $n=106$  focal adhesions. d) Mean intensity of vinculin at the cell-cell junction in the middle plane ( $n=54$ ). e) Distribution of YAP in nucleus, cytoplasm, or uniform distribution calculated for  $n=1162$  cells (MDCK WT) and  $n=1008$  cells (MDCK E-cadherin KO). Error bars represent the standard deviation. Unpaired t-test was performed leading to  $*p<0.05$ ,  $**p<0.01$ ,  $***p<0.001$  and  $****p<0.0001$ . Scale bars, 20 $\mu$ m.

**Figure 5| Cell sorting triggered by change in nematic behaviour of monolayers.**

a,b) Time lapse sorting of extensile and contractile cells observed over time represented by mixing index in simulations (a) and experiments (b) of MDCK WT (magenta) and E-cadherin KO cells tagged with LifeAct GFP (green). In (a)  $\zeta_s/R\alpha = 0.042$ ,  $\zeta_Q/R\alpha = -0.062$  for the extensile cells and  $\zeta_s/R\alpha = 0.0$ ,  $\zeta_Q/R\alpha = -0.062$  for the contractile cells. Mixing index was obtained from two independent simulations and the error bars mark the standard deviation. Mixing index in experiments (b) was obtained from  $n=5$  different clusters from 2 independent samples. Error bars represent the standard deviation. Scale bars: 100 $\mu$ m.

**Figure 6| Cell sorting is governed by activity of the system.**

a) Demixing of MDCK WT and E-cadherin KO at different starting densities, WT (30%) and E-cadherin KO (70%) (left) and WT (70%) and E-cadherin KO (30%) (right). b) Demixing of extensile and contractile particles obtained from simulations at different starting densities. Extensile and contractile particles are mixed at 50-50 (left), 30-70 (middle) and 70-30 (right) respectively. In (b)  $\zeta_s/R\alpha = 0.016$ ,  $\zeta_Q/R\alpha = -0.016$  for the extensile cells and  $\zeta_s/R\alpha = 0.0$ ,  $\zeta_Q/R\alpha = -0.016$  for the contractile cells. c) Demixing phase observed before and after the addition of 20 $\mu$ M blebbistatin characterized by mixing index (left) ( $n=5$ ) and circularity of several colonies (right) ( $n=5$ ). Error bars represent the standard deviation. Scale bars: 100 $\mu$ m.

# Figure 1

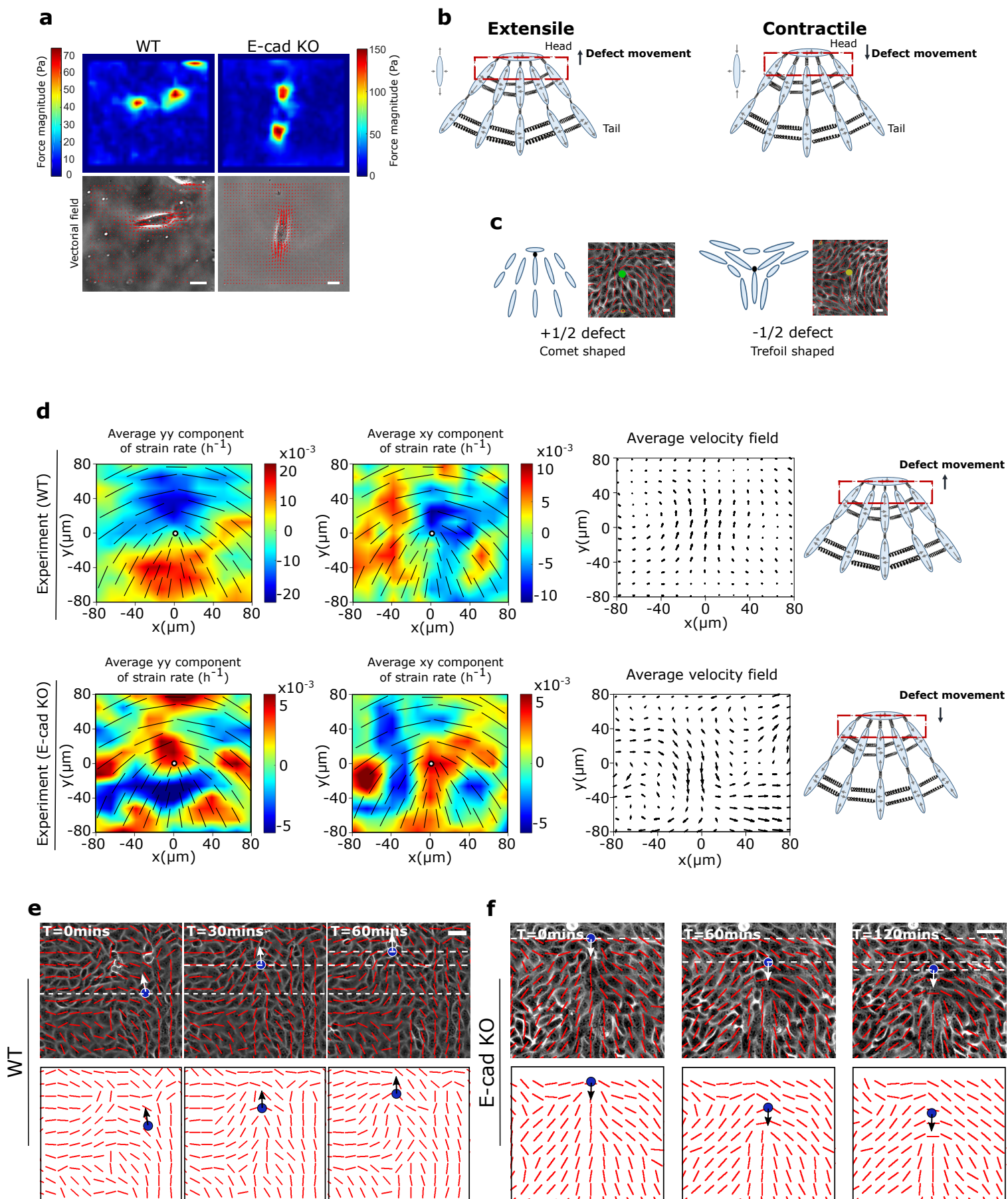


# Figure 2

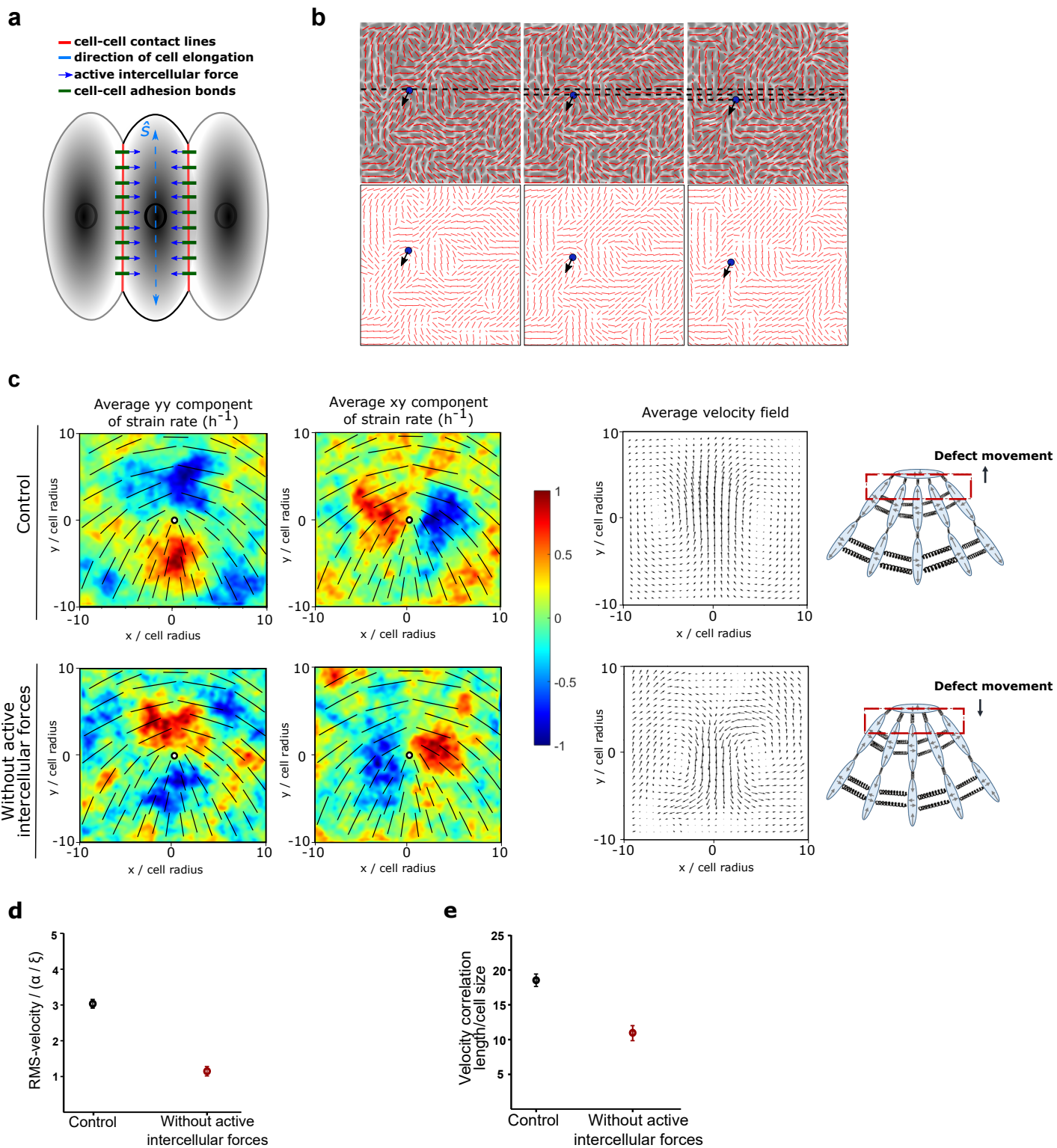


# Figure 3

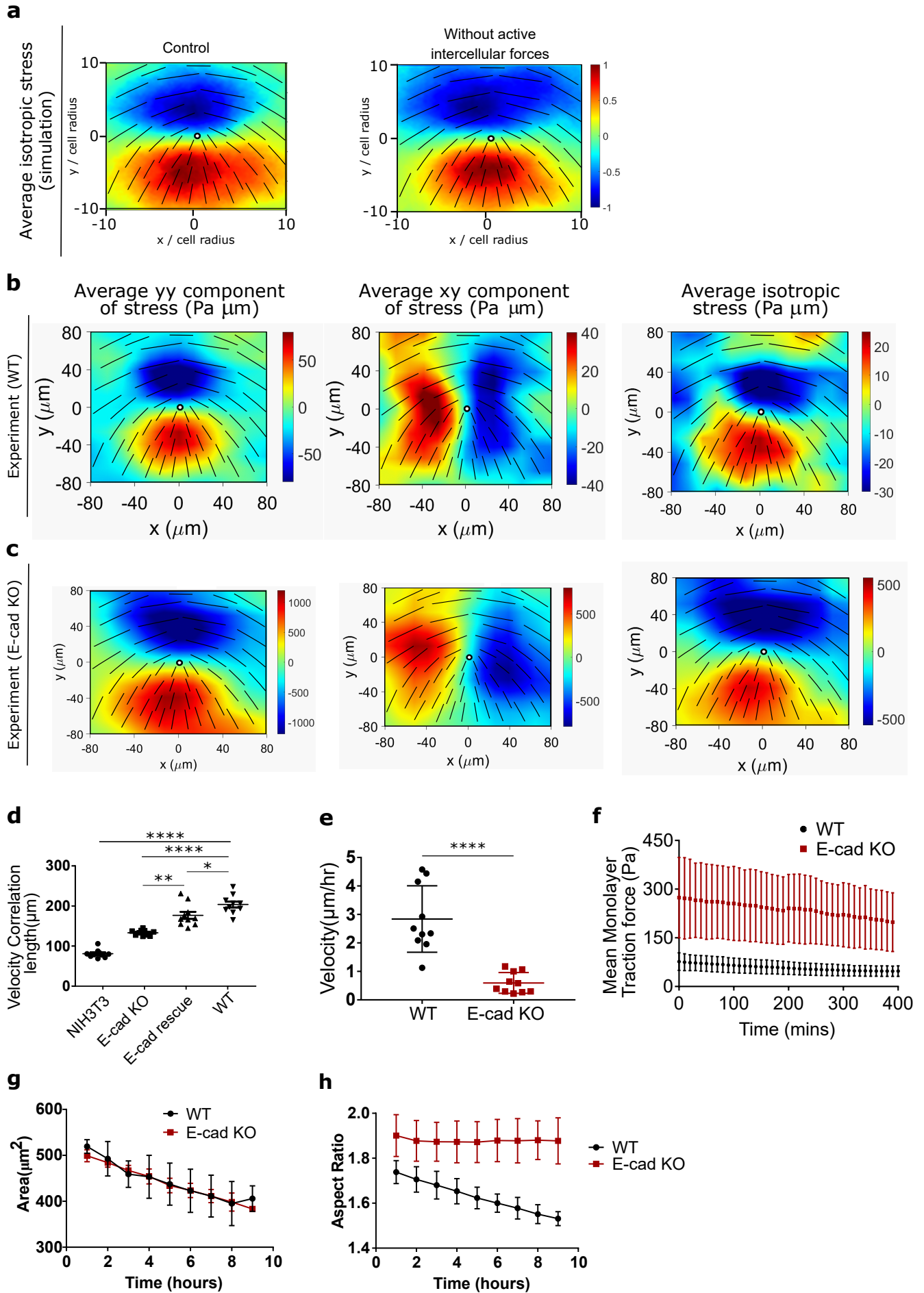


# Figure 4

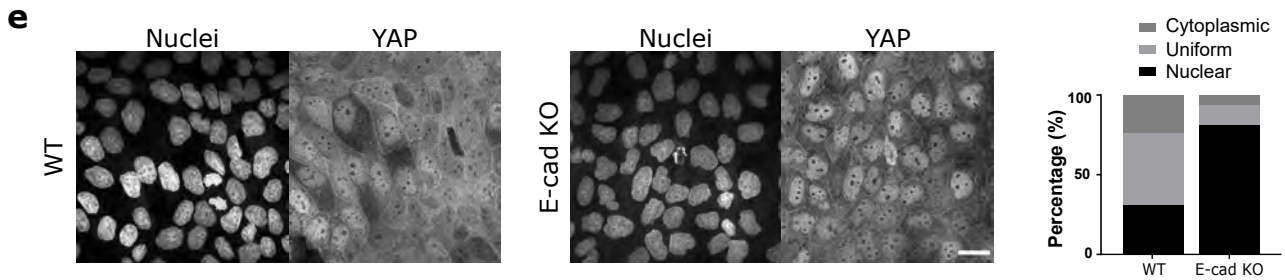
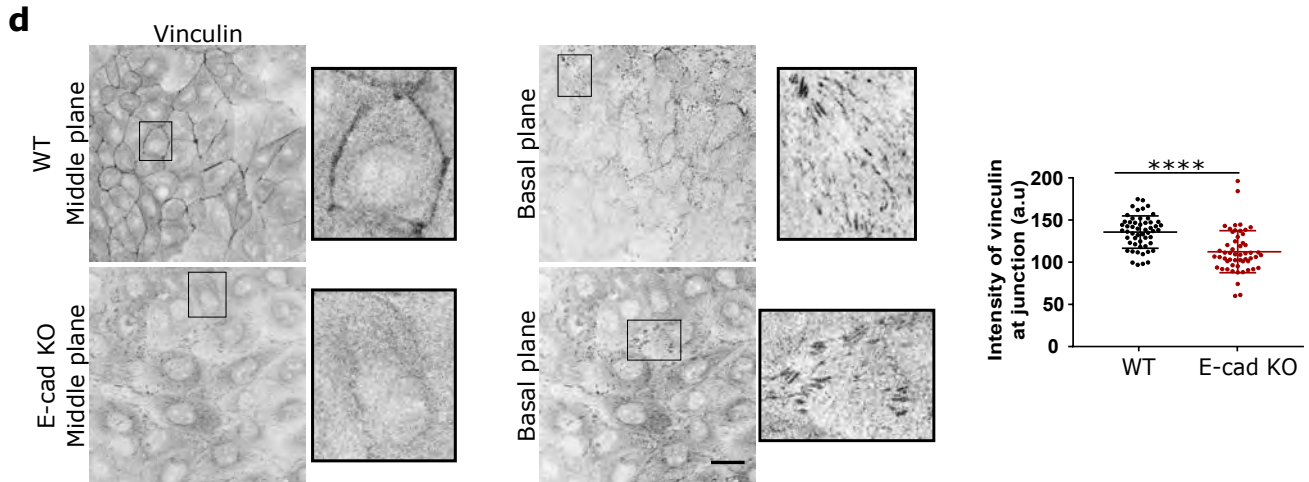
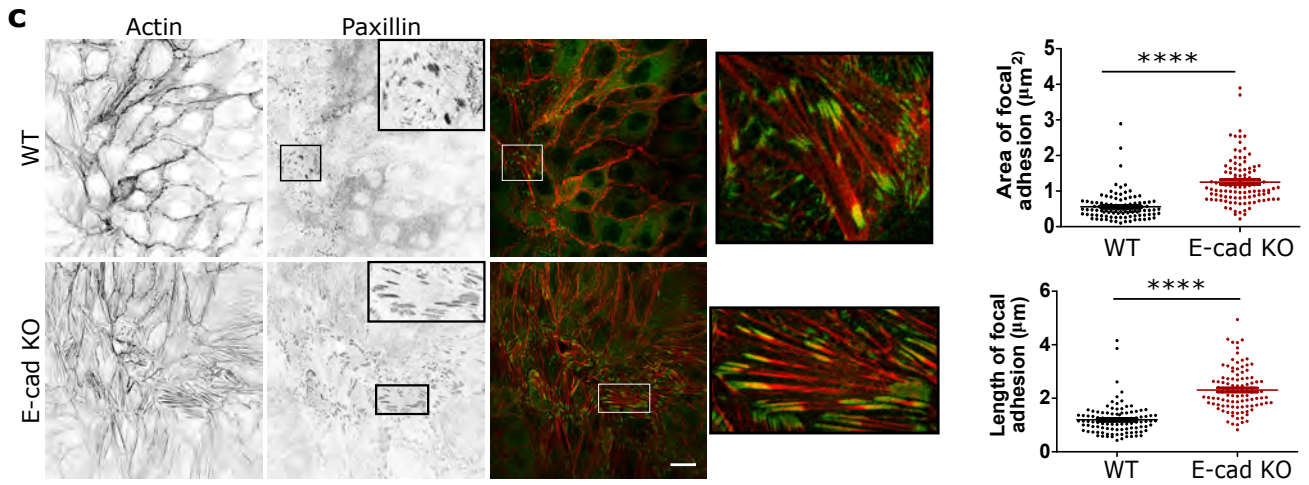
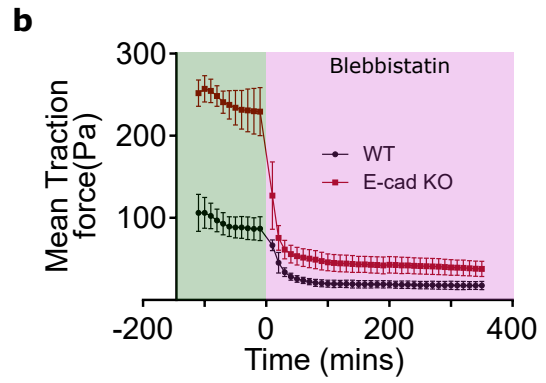
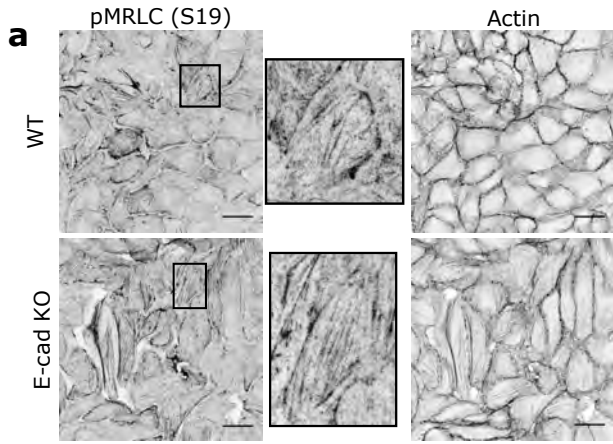


# Figure 5

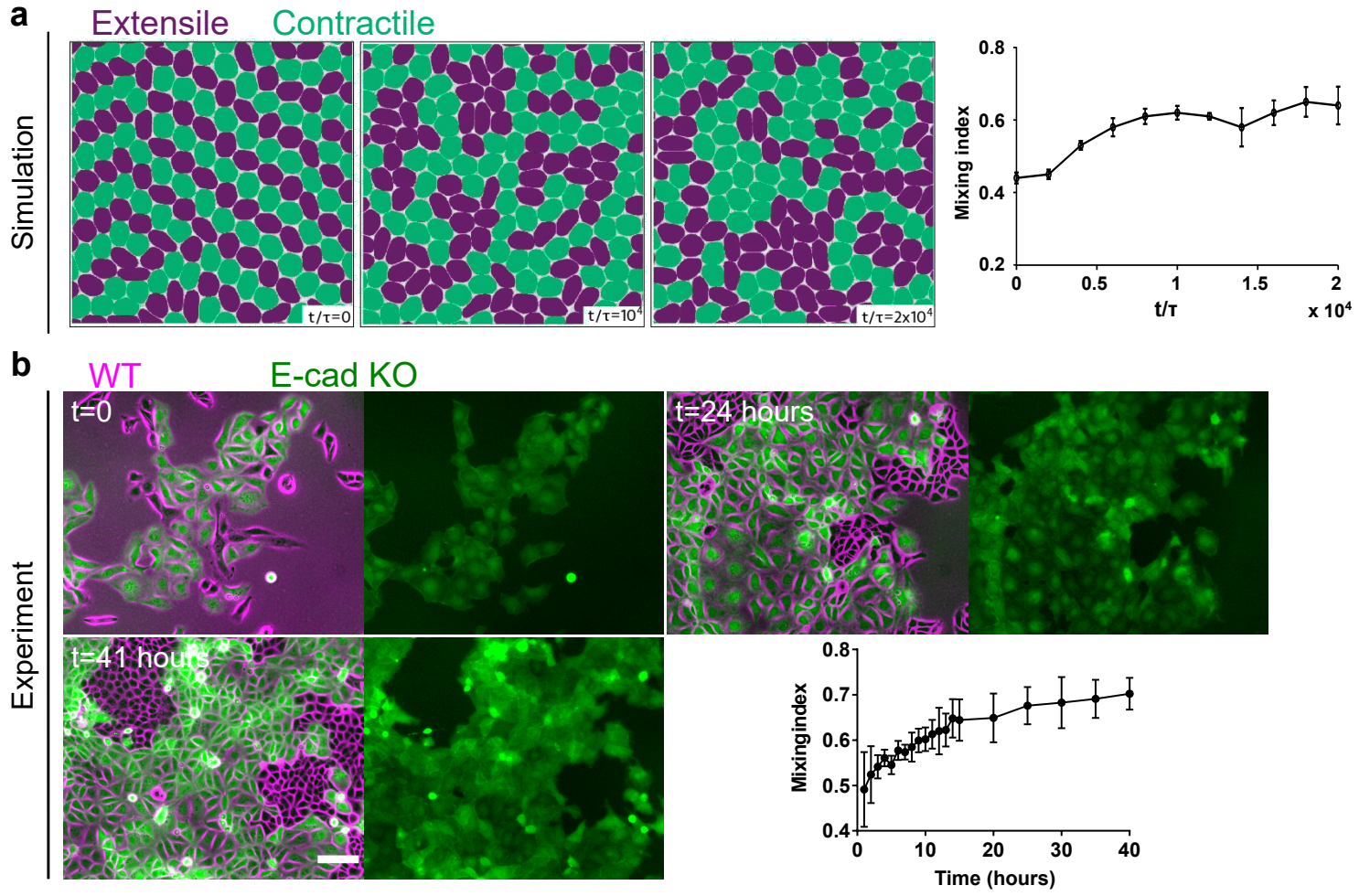


# Figure 6

